

OBSERVATION OF HIGGS BOSON DECAY TO BOTTOM QUARKS  
WHEN PRODUCED IN ASSOCIATION WITH A WEAK VECTOR BOSON

By

SEAN-JIUN WANG

A DISSERTATION PRESENTED TO THE GRADUATE SCHOOL  
OF THE UNIVERSITY OF FLORIDA IN PARTIAL FULFILLMENT  
OF THE REQUIREMENTS FOR THE DEGREE OF  
DOCTOR OF PHILOSOPHY

UNIVERSITY OF FLORIDA

2019

© 2019 Sean-Jiun Wang

For my parents, who abandoned the familiar comforts of Taiwan and came to the United States because they wanted the best for their future children.

## ACKNOWLEDGMENTS

I want to first and foremost thank Jacobo Konigsberg for giving me the opportunity to work and learn under his guidance. Because of this, I was able to contribute to a long-awaited and historic result at the cutting edge of the field. I could not have asked for a better advisor, and I will cherish his invaluable support and instruction. I also want to thank Ivan Furic and Darin Acosta for providing undergraduate research opportunities that inspired my continued work on the CMS experiment and awakened my interest in machine learning. As our research is made possible by the University of Florida and the U.S. Department of Energy, I thank them for their support.

I also want to recognize and thank the CMS collaboration and those involved in LHC operations, whose tireless work continues to produce datasets of epic size that are a joy to explore. During my time at CERN, the Cookman's welcomed me into their home and I am grateful for their hospitality. I also thank the colleagues and office mates who enriched my time at Fermilab, specifically Souvik Das, Jia Fu Low, and Caterina Vernieri. Such a challenging analysis wouldn't have been a success without the shared vision and expertise of the  $VH(b\bar{b})$  analysis team, so I thank and congratulate my closest colleagues on the job well done. Special thanks go to Michele de Gruttola and Christopher Palmer for their mentorship.

I thank my family for their endless love and encouragement and for giving me the freedom to choose how I might make the world a better place. I also thank my wife, Gwynndolyn, who has shown amazing patience and understanding while I travelled around the world chasing particles. I am forever grateful for her love and sacrifice which has allowed me to pursue my research. And finally, I thank God, who after creating the whirling cosmos saw fit to fashion humanity with the means to not only perceive its beauty but also fathom its design.

## TABLE OF CONTENTS

	<u>page</u>
ACKNOWLEDGMENTS . . . . .	4
LIST OF TABLES . . . . .	7
LIST OF FIGURES . . . . .	8
ABSTRACT . . . . .	9
 CHAPTER	
1 INTRODUCTION . . . . .	10
1.1 The Standard Model . . . . .	10
1.1.1 Fermions . . . . .	11
1.1.2 Bosons . . . . .	12
1.1.3 The Higgs Mechanism . . . . .	13
1.1.3.1 Gauge boson masses . . . . .	15
1.1.3.2 Fermion masses . . . . .	17
1.2 The Higgs Boson . . . . .	20
1.2.1 Phenomenology . . . . .	20
1.2.1.1 Production modes . . . . .	21
1.2.1.2 Decay modes . . . . .	24
1.2.2 Discovery . . . . .	26
1.3 Searches for $VH(b\bar{b})$ . . . . .	26
1.3.1 Motivation for $VH(b\bar{b})$ . . . . .	27
1.3.2 Previous Results . . . . .	30
2 EXPERIMENTAL APPARATUS . . . . .	32
2.1 The Large Hadron Collider . . . . .	33
2.2 The Compact Muon Solenoid . . . . .	37
2.2.1 Detector Subsystems . . . . .	41
2.2.1.1 Silicon Tracker . . . . .	42
2.2.1.2 Electromagnetic Calorimeter . . . . .	42
2.2.1.3 Hadronic Calorimeter . . . . .	42
2.2.1.4 The Muon Subsystems . . . . .	42
2.2.2 Data Acquisition and Triggers . . . . .	42
2.2.2.1 Level 1 trigger . . . . .	42
2.2.2.2 High level trigger . . . . .	42
2.2.3 Computing . . . . .	42
2.2.4 Upgrades for Run 2 . . . . .	42

<b>3</b>	<b>ANALYSIS STRATEGY . . . . .</b>	<b>43</b>
<b>3.1</b>	<b>Data and Simulation . . . . .</b>	<b>43</b>
<b>3.1.1</b>	<b>Residual Monte-Carlo Corrections . . . . .</b>	<b>43</b>
<b>3.2</b>	<b>Vector Boson Reconstruction . . . . .</b>	<b>43</b>
<b>3.3</b>	<b>Higgs Boson Reconstruction . . . . .</b>	<b>43</b>
<b>3.4</b>	<b>Event Selection . . . . .</b>	<b>43</b>
<b>3.4.1</b>	<b>Signal Regions . . . . .</b>	<b>43</b>
<b>3.4.2</b>	<b>Background Control Regions . . . . .</b>	<b>43</b>
<b>3.5</b>	<b>Binned Multivariate Shape Analysis . . . . .</b>	<b>43</b>
<b>3.5.1</b>	<b>Input Features . . . . .</b>	<b>43</b>
<b>3.5.2</b>	<b>Model Training . . . . .</b>	<b>43</b>
<b>3.5.3</b>	<b>Model Selection . . . . .</b>	<b>43</b>
<b>3.5.4</b>	<b>Binned Shape Analysis . . . . .</b>	<b>43</b>
<b>3.6</b>	<b>Systematic Uncertainties . . . . .</b>	<b>43</b>
<b>APPENDIX</b>		
<b>A</b>	<b>EVENT DISPLAYS . . . . .</b>	<b>44</b>
<b>REFERENCES . . . . .</b>		<b>50</b>
<b>BIOGRAPHICAL SKETCH . . . . .</b>		<b>52</b>

## LIST OF TABLES

<u>Table</u>	<u>page</u>
1-1 Production Cross Sections for the Higgs Boson and SM Background Process at the LHC . . . . .	31
A-1 Event Display Candidate Information . . . . .	44

## LIST OF FIGURES

<u>Figure</u>		<u>page</u>
1-1 Standard Model Infographic . . . . .	11	
1-2 Shape of the Higgs Field Potential . . . . .	14	
1-3 Higgs Boson Interaction Vertices . . . . .	21	
1-4 Higgs Boson Production Cross Sections . . . . .	22	
1-5 Higgs Boson Production Diagrams . . . . .	23	
1-6 Higgs Boson Branching Ratios . . . . .	25	
1-7 Production Cross Sections at the LHC . . . . .	28	
1-8 CMS Measurements of SM Production Cross Sections . . . . .	29	
1-9 $VH(b\bar{b})$ Background Process Diagrams . . . . .	29	
2-1 Overall View of the LHC . . . . .	33	
2-2 CERN Accelerator Complex . . . . .	35	
2-3 LHC Dipole and Quadrupole Magnets . . . . .	35	
2-4 Cutaway View of the CMS Detector . . . . .	38	
2-5 Sagitta of a Charged Particle Track . . . . .	39	
2-6 Coordinate System of the CMS Detector . . . . .	41	
2-7 Cross Sectional View of the CMS Detector . . . . .	42	
A-1 Event Display for $Z(\nu\bar{\nu})H(b\bar{b})$ Candidate . . . . .	45	
A-2 Event Display for $W(e\nu)H(b\bar{b})$ Candidate . . . . .	46	
A-3 Event Display for $W(\mu\nu)H(b\bar{b})$ Candidate . . . . .	47	
A-4 Event Display for $Z(e\bar{e})H(b\bar{b})$ Candidate . . . . .	48	
A-5 Event Display for $Z(\mu\bar{\mu})H(b\bar{b})$ Candidate . . . . .	49	

Abstract of Dissertation Presented to the Graduate School  
of the University of Florida in Partial Fulfillment of the  
Requirements for the Degree of Doctor of Philosophy

OBSERVATION OF HIGGS BOSON DECAY TO BOTTOM QUARKS  
WHEN PRODUCED IN ASSOCIATION WITH A WEAK VECTOR BOSON

By

Sean-Jiun Wang

May 2019

Chair: Jacobo Konigsberg

Cochair: Ivan K. Furic

Major: Physics

A search for the Standard Model Higgs boson ( $H$ ) produced in association with a weak vector boson ( $VH$ ) and decaying into a bottom-antibottom quark pair ( $b\bar{b}$ ) is reported for the decay channels  $Z(\nu\bar{\nu})H(b\bar{b})$ ,  $W(e\nu)H(b\bar{b})$ ,  $W(\mu\nu)H(b\bar{b})$ ,  $Z(e\bar{e})H(b\bar{b})$ , and  $Z(\mu\bar{\mu})H(b\bar{b})$ , with a focus on  $Z(\nu\bar{\nu})H(b\bar{b})$  in particular. The search is performed with a dataset corresponding to an integrated luminosity of  $41.3 \text{ fb}^{-1}$  at a center-of-mass energy of  $\sqrt{s} = 13 \text{ TeV}$  recorded by the CMS experiment at the LHC during Run 2 in 2017. An excess of events is observed above the expected background with a significance of 3.3 standard deviations, which is compatible with the Standard Model expectation of 3.1 standard deviations for a Higgs boson of mass  $m_H = 125.09 \text{ GeV}$ . When combined with the results of previous  $VH$  measurements and  $H \rightarrow b\bar{b}$  searches using other Higgs production modes, the observed (expected) significance is 5.6 (5.5) standard deviations. This represents the first observation of  $H \rightarrow b\bar{b}$  by the CMS experiment.

## CHAPTER 1

### INTRODUCTION

The fundamental structure of the universe has remained an enduring fascination of mankind. The philosophers of antiquity speculated that the world could be decomposed into the base elements of water, earth, fire, and air. The alchemists of the Middle Ages, regarding the classical elements to be expressions of hidden substance, sought to unveil its nature with crude experiments. The scholars of the Renaissance rejected the Aristotelian description of physical phenomena for its empirical failures and pondered if atoms were the indivisible units of matter. The chemists of the 19th century advanced and refined the atomic theory in their pursuit to catalog the pure elements. The physicists of the 20th century realized the necessity of a quantum description of the universe while delving into the subatomic realm. The scientific paradigm of the current era now rests on the theoretical framework known as the Standard Model of particle physics which, though understood to be incomplete, has had its predictions verified with remarkable accuracy.

#### 1.1 The Standard Model

The fundamental forces<sup>1</sup> and forms of matter within the universe are explained by the Standard Model in terms of elementary particles, their antiparticles, and their interactions. The following subsections highlight the features of the model necessary to motivate the treatise of this paper. A formal and rigorous treatment of the theory is beyond the scope of this paper but may be found in such texts as Ref. [1] and [2].

The Standard Model is a relativistic quantum field theory (QFT) in which fundamental particles are understood to be excitations of their associated fields that permeate all of space-time. The fundamental forces are generated by the internal gauge symmetry of the model  $SU(3) \times SU(2) \times U(1)$ , which gives rise to the strong ( $SU(3)$ ), weak ( $SU(2)$ ),

---

<sup>1</sup> Gravity, which does not have a satisfactory quantum description, falls outside of the Standard Model.

and electromagnetic ( $U(1)$ ) interactions. Its current formulation is thus a combination of electroweak theory with quantum chromodynamics (QCD). The particles manifested by the model may be broadly categorized into *fermions* and *bosons* and a visual summary is shown in Figure 1-1.

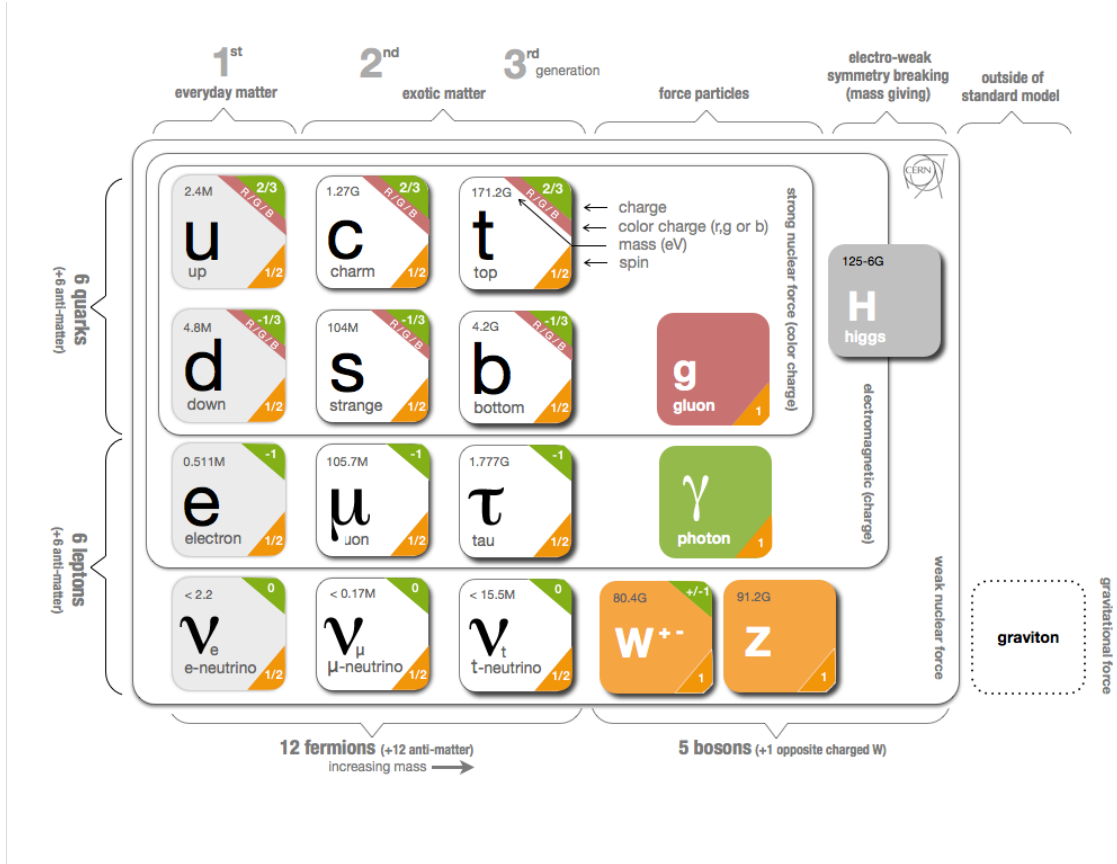


Figure 1-1. An infographic of the Standard Model [3]. The elementary particles are arranged in their usual generational pairs and the surrounding solid lines divide them into sections based on the fundamental forces they experience.

### 1.1.1 Fermions

The fermions encompass all forms of ordinary and exotic matter and obey Fermi-Dirac statistics because of their half-integer spin, namely, spin- $\frac{1}{2}$ . They are divided into *leptons* and *quarks*. The electrically charged leptons interact via the electromagnetic and weak nuclear forces and include the familiar *electron* ( $e$ ), the *muon* ( $\mu$ ), and the *tau* ( $\tau$ ). The charged leptons also have neutral counterparts ( $\nu_e$ ,  $\nu_\mu$ ,  $\nu_\tau$ ) known as *neutrinos*, which

interact solely via the weak nuclear force. The quarks, having both electric and color charge, interact via the electromagnetic and strong and weak nuclear forces and include the up ( $u$ ), down ( $d$ ), charm ( $c$ ), strange ( $s$ ), bottom ( $b$ ), and top ( $t$ ). Although the leptons can exist freely, the nature of the strong interaction gives rise to color confinement, whereby quarks only appear within composite particles called hadrons. The bound states of quark doublets are known as mesons while those of quark triplets, of which the familiar proton is an example, are known as baryons.

The leptons and quarks are each arranged into pairs by flavour quantum number and sorted into three generations of increasing mass<sup>2</sup>, as depicted in Figure 1-1. The more massive particles of the higher generations decay into the stable particles of the first generation, which corroborates the observation that ordinary matter consists of electrons and up and down quarks which are bound in protons and neutrons. There are no known constraints on the number of fermion generations, although experimental results suggest there are only three.

### 1.1.2 Bosons

The bosons, which obey Bose-Einstein statistics because of their integer spin, are divided into vector and scalar bosons. The spin-1 vector, or gauge, bosons mediate the fundamental forces and are exchanged between elementary particles during their interactions. The photon ( $\gamma$ ) mediates the electromagnetic force, which is responsible for the phenomenon of intermolecular repulsion.<sup>3</sup> The  $W$  and  $Z$  bosons mediate the weak nuclear force that causes nuclear decay. And finally, the gluons ( $g$ ) mediate the strong nuclear force that binds quarks into hadrons and even protons and neutrons in nuclei. The

---

<sup>2</sup> The observation of neutrino oscillations disproved the prediction that they are massless but its implications for the lepton generations are unclear.

<sup>3</sup> It is this repulsion that prevents us from passing through objects.

only spin-0 scalar boson in the theory is the Higgs boson ( $H$ ), which is responsible for the masses of the heavy gauge bosons and fermions.

### 1.1.3 The Higgs Mechanism

The requirement of gauge invariance under  $SU(2)$  leads to a prediction of massless gauge bosons, which stands in contrast to the observation that the weak vector bosons are massive. In order to reconcile this observation while preserving the gauge invariance of the interaction, a mechanism of *spontaneous symmetry breaking* was incorporated into the unified electroweak theory proposed by Sheldon Glashow [4], Abdus Salam [5], and Steven Weinberg [6]. This mechanism, which came to be known as the *Higgs mechanism*, was independently developed by Robert Brout and François Englert [7], its namesake Peter Higgs [8], and Gerald Guralnik, Richard Hagen, and Sir Thomas Kibble [9].

The mechanism introduces into the Standard Model a scalar field  $\phi$  represented as a complex doublet

$$\phi = \begin{pmatrix} \phi^+ \\ \phi^0 \end{pmatrix} = \frac{1}{\sqrt{2}} \begin{pmatrix} \phi_1 + i\phi_2 \\ \phi_3 + i\phi_4 \end{pmatrix} \quad (1-1)$$

and its potential  $V(\phi)$  of the form

$$V(\phi) = \mu^2 \phi^\dagger \phi + \frac{\lambda}{2} (\phi^\dagger \phi)^2, \quad (1-2)$$

where the real parameters  $\mu^2$  and  $\lambda$  represent the mass and self-coupling, respectively. The self-coupling  $\lambda$  is taken to be positive by convention such that the potential is bounded from below. When  $\mu^2 > 0$ , the potential is parabolic in shape and the ground state of the vacuum is at  $\phi = 0$ , keeping its symmetries intact. However, when  $\mu^2 < 0$ , the minimum of the potential is no longer at  $\phi = 0$  but rather<sup>4</sup>

$$v = \left( \frac{-\mu^2}{\lambda} \right)^{1/2}, \quad (1-3)$$

---

<sup>4</sup> The solution is unique up to a phase  $e^{i\theta}$ , but it is customary to take  $\theta = 0$ .

where the vacuum now attains an expectation value  $v$  in its ground state. The shape of such a potential is illustrated in Figure 1-2. The Higgs mechanism thus provides the means to spontaneously break the  $SU(2) \times U(1)$  symmetry within the model.

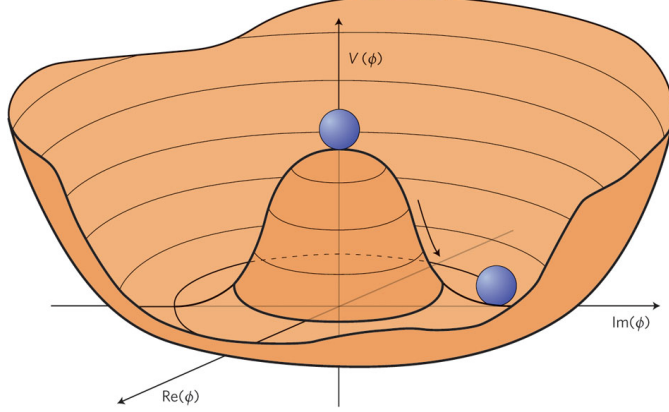


Figure 1-2. The shape of the Higgs field potential for  $\mu^2 < 0$  [10]. The transition of the field from its unstable state at the origin to its true ground state spontaneously breaks the rotational symmetry of the system.

Because particles are excitations of their fields, the presence of the Higgs field also suggests the existence of the Higgs boson. An expression for the mass of this new boson can be determined by expanding the potential around the vacuum ground state  $\phi_0$ . By choosing the unitary gauge, the components of  $\phi_0$  become

$$(\phi_1)_0 = 0, (\phi_2)_0 = 0, (\phi_3)_0 = v, (\phi_4)_0 = 0 \quad (1-4)$$

and  $\phi_0$  becomes simply

$$\phi_0 = \begin{pmatrix} \phi^+ \\ \phi^0 \end{pmatrix}_0 = \frac{1}{\sqrt{2}} \begin{pmatrix} 0 \\ v \end{pmatrix}. \quad (1-5)$$

Then for small fluctuations  $\phi(x) = \phi_0 + H(x)$ , the potential to second order in  $H$  becomes

$$\begin{aligned} V(\phi) &= \frac{\mu^2}{2}(v^2 + 2vH + H^2) + \frac{\lambda}{4}(v^2 + 2vH + H^2)^2 \\ &= \frac{1}{2}(\mu^2 v^2 + \frac{\lambda}{2}v^4) + (\mu^2 v + \lambda v^3)H + \frac{1}{2}(\mu^2 + 3\lambda v^2)H^2 + \mathcal{O}(H^3) \\ &= V_0 - \frac{1}{2}(2\mu^2)H^2 + \mathcal{O}(H^3), \end{aligned} \quad (1-6)$$

where  $V_0$  collects the constant terms and Equation 1-3 has been used to vanish the first order term and simplify the second order term. The mass can be read from the coefficient of the second order term in  $H$ :

$$m_H^2 = -2\mu^2 \implies m_H = \sqrt{2}\mu = \sqrt{2\lambda}v, \quad (1-7)$$

where the sign of the mass was dropped because  $\mu^2$  was chosen to be negative. Although the Standard Model predicts a massive Higgs boson, its dependence on the value of the unknown self-coupling parameter  $\lambda$  and the vacuum expectation value  $v$  means it must be determined experimentally.

### 1.1.3.1 Gauge boson masses

The necessity of the Higgs mechanism is realized by how it generates the masses of the gauge bosons. The Lagrangian for the Higgs may be written as

$$\mathcal{L}_\phi = (D_\mu\phi)^\dagger(D^\mu\phi) - V(\phi) = (D_\mu\phi)^\dagger(D^\mu\phi) - \mu^2\phi^\dagger\phi - \frac{\lambda}{2}(\phi^\dagger\phi)^2, \quad (1-8)$$

By definition, the Higgs field has weak hypercharge  $Y = +1$  and weak isospin  $T_3 = -1/2$ . The weak hypercharge  $Y$  and weak isospin  $T$  are the generators of the SU(2) and U(1) symmetries, respectively, with the choice of their values made to satisfy the relation

$$Q = T_3 + \frac{1}{2}Y, \quad (1-9)$$

where  $Q$  is the electric charge.<sup>5</sup> These choices require the covariant derivative of the kinetic term to be of the form

$$D_\mu\phi = (\partial_\mu - \frac{i}{2}g\boldsymbol{\sigma} \cdot \mathbf{W}_\mu - \frac{i}{2}g'B_\mu)\phi, \quad (1-10)$$

where  $\mathbf{W}_\mu$  and  $B_\mu$  are, respectively, the SU(2) and U(1) gauge bosons,  $g$  and  $g'$  are the corresponding gauge couplings, and  $\boldsymbol{\sigma} = \sigma^a, a = 1, 2, 3$  are the Pauli matrices.

---

<sup>5</sup> Hence, the Higgs boson is a neutral particle.

The gauge boson masses are contained in the kinetic term of the Lagrangian and can be determined by evaluating its expression for the vacuum ground state. The covariant derivative becomes

$$\begin{aligned} D_\mu \phi &\rightarrow \left[ \partial_\mu - \frac{i}{2}g \begin{pmatrix} W_\mu^3 & W_\mu^1 - iW_\mu^2 \\ W_\mu^1 + iW_\mu^2 & -W_\mu^3 \end{pmatrix} - \frac{i}{2}g' B_\mu \right] \frac{1}{\sqrt{2}} \begin{pmatrix} 0 \\ v + H \end{pmatrix} \\ &= -\frac{i}{2} \begin{pmatrix} \frac{g}{\sqrt{2}}(W_\mu^1 - iW_\mu^2)(v + H) \\ i\sqrt{2}\partial_\mu H + \frac{1}{\sqrt{2}}(-gW_\mu^3 + g'B_\mu)(v + H) \end{pmatrix} \end{aligned} \quad (1-11)$$

and substituting this expression into Equation 1-8 while ignoring the potential term for clarity yields

$$\begin{aligned} \mathcal{L}_\phi &= \frac{1}{4} \left| \begin{pmatrix} \frac{g}{\sqrt{2}}(W_\mu^1 - iW_\mu^2)(v + H) \\ i\sqrt{2}\partial_\mu H + \frac{1}{\sqrt{2}}(-gW_\mu^3 + g'B_\mu)(v + H) \end{pmatrix} \right|^2 \\ &= \frac{1}{4} \left[ 2(\partial_\mu H)^2 + \left( \frac{g^2}{2} ((W_\mu^1)^2 + (W_\mu^2)^2) + \frac{1}{2} (g'B_\mu - gW_\mu^3)^2 \right) (v + H)^2 \right] \\ &= \frac{1}{2}(\partial_\mu H)^2 + \frac{g^2}{8}(W_\mu^1)^2 v^2 + \frac{g^2}{8}(W_\mu^2)^2 v^2 + \frac{1}{8} (g'B_\mu - gW_\mu^3)^2 v^2 + \mathcal{O}(H), \end{aligned} \quad (1-12)$$

where higher order terms in  $H$  have been discarded. The result of Equation 1-12 reveals that the broken symmetry of the Higgs field causes the  $W_\mu^1$  and  $W_\mu^2$  vector fields to both acquire a mass of

$$m_W^2 = \frac{g^2 v^2}{4} \implies m_W = \frac{gv}{2}. \quad (1-13)$$

The linear combination of vector fields  $(g'B_\mu - gW_\mu^3)$  also acquires a mass that depends on the couplings  $g$  and  $g'$ , and is typically expressed as

$$m_Z^2 = \frac{(g^2 + g'^2)v^2}{4} \implies m_Z = \frac{\sqrt{g^2 + g'^2}v}{2}. \quad (1-14)$$

The excitations of these massive vector fields are the weak gauge bosons  $W^+$ ,  $W^-$ , and  $Z^0$  which have been observed in nature and whose masses have been measured[11] to be

$$m_{W^+} = m_{W^-} = 80.379 \pm 0.012 \text{ GeV} \text{ and } m_{Z^0} = 91.1876 \pm 0.0021 \text{ GeV}. \quad (1-15)$$

The derivation would be complete but for a missing gauge boson. Recall our earlier transformation to the unitary gauge which fixed three of the four degrees of freedom of the Higgs field. According to Goldstone's Theorem[12], these degrees of freedom become the longitudinal polarizations of the now massive weak gauge bosons. The untouched degree of freedom thus corresponds to the massless photon  $\gamma$ . By taking the electromagnetic field  $A_\mu$  to be proportional to the missing linear combination of fields ( $g'W_\mu^3 + gB_\mu$ ), it can be explicitly introduced into the kinetic term of the Lagrangian while remaining orthogonal to the other fields.

### 1.1.3.2 Fermion masses

Although the Dirac Lagrangian describes the dynamics of the fermions, it is inadequate for explaining their observed masses. This is because a Dirac mass term of the form

$$m\bar{\psi}\psi = m(\bar{\psi}_L + \bar{\psi}_R)(\psi_L + \psi_R) = m(\bar{\psi}_L\psi_R + \bar{\psi}_R\psi_L) \quad (1-16)$$

violates the gauge invariance of the model by coupling together left-handed and right-handed fermions which transform differently under both SU(2) and U(1). The masses of the fermions are instead another consequence of spontaneous symmetry breaking, and their coupling to the scalar Higgs field through Yukawa interactions gives rise to their mass terms in the Standard Model Lagrangian.

The Yukawa interaction of the first generation leptons to the Higgs field  $\phi$  is given by

$$\mathcal{L}_{\text{Yukawa}} = -\lambda_e (\bar{L}\phi e_R + \bar{e}_R\phi^\dagger L), \quad (1-17)$$

where  $\lambda_e$  is the coupling constant, the SU(2) singlet  $e_R$  represents the right-handed electron, and the SU(2) doublet  $L$  represents the left-handed neutrino<sup>6</sup> and electron, i.e.

$$L = \begin{pmatrix} \nu_L \\ e_L \end{pmatrix}. \quad (1-18)$$

Evaluating this expression for the vacuum ground state yields the electron mass term

$$\begin{aligned} \mathcal{L}_{\text{Yukawa}} &= -\lambda_e \left( \bar{L} \phi_0 e_R + \bar{e}_R \phi_0^\dagger L \right) \\ &= -\frac{\lambda_e}{\sqrt{2}} \left[ \begin{pmatrix} \bar{\nu}_L & \bar{e}_L \end{pmatrix} \begin{pmatrix} 0 \\ v \end{pmatrix}_0 e_R + \bar{e}_R \begin{pmatrix} 0 & v \end{pmatrix}_0 \begin{pmatrix} \nu_L \\ e_L \end{pmatrix} \right] \\ &= -\frac{\lambda_e v}{\sqrt{2}} (\bar{e}_L e_R + \bar{e}_R e_L), \end{aligned} \quad (1-19)$$

which gives the electron mass

$$m_e = \frac{\lambda_e v}{\sqrt{2}}. \quad (1-20)$$

Therefore the electron, and similarly for the charged leptons of the other generations, is a mixture of left-handed and right-handed fields which acquire a mass that is proportional to the vacuum expectation value  $v$  and their coupling to the Higgs field.

The Yukawa interaction of the quarks, taking into account the existence of the right-handed SU(2) singlet  $u_R$ , is similarly given by

$$\mathcal{L}_{\text{Yukawa}} = -\Lambda_d^{ij} (\bar{Q}_L^i \phi d_R^j + \bar{d}_R^j \phi^\dagger Q_L^i) - \Lambda_u^{ij} (\bar{Q}_L^i \tilde{\phi} u_R^j + \bar{u}_R^j \tilde{\phi}^\dagger Q_L^i), \quad (1-21)$$

where  $\Lambda_d^{ij}$  and  $\Lambda_u^{ij}$  are  $3 \times 3$  complex matrices of couplings for the down-type and up-type quarks, respectively, whose indices  $i$  and  $j$  run over the quark generations,  $d_R$  and  $u_R$  are

<sup>6</sup> The neutrinos have been experimentally measured, within uncertainties, to have left-handed helicity only.

the right-handed singlets,  $Q_L$  is the left-handed doublet

$$Q_L = \begin{pmatrix} u_L \\ d_L \end{pmatrix}, \quad (1-22)$$

and  $\tilde{\phi}$  is the charge conjugate of the Higgs doublet

$$\tilde{\phi} = \begin{pmatrix} \phi^{0*} \\ -\phi^{+*} \end{pmatrix} \implies \tilde{\phi}_0 = \begin{pmatrix} v \\ 0 \end{pmatrix}. \quad (1-23)$$

Proceeding as before, evaluating this expression for the vacuum ground state yields

$$\mathcal{L}_{\text{Yukawa}} = -\frac{v}{\sqrt{2}} \Lambda_d^{ij} (\bar{d}_L^i d_R^j + \bar{d}_R^j d_L^i) - \frac{v}{\sqrt{2}} \Lambda_u^{ij} (\bar{u}_L^i u_R^j + \bar{u}_R^j u_L^i), \quad (1-24)$$

from which the quark masses are found to be

$$M_d^{ij} = \frac{\Lambda_d^{ij} v}{\sqrt{2}} \text{ and } M_u^{ij} = \frac{\Lambda_u^{ij} v}{\sqrt{2}}. \quad (1-25)$$

These mass terms resemble those of leptons except that they are matrices which depend on the Yukawa couplings of the mixed quark states to the Higgs field. The physical quark fields correspond to the mass eigenstates obtained by diagonalizing the mass matrices  $M_d^{ij}$  and  $M_u^{ij}$ . A general complex matrix may be diagonalized by a biunitary transformation, so there exist unitary matrices  $\mathbf{D}_L$ ,  $\mathbf{D}_R$ ,  $\mathbf{U}_L$ , and  $\mathbf{U}_R$  such that

$$\mathbf{D}_L^\dagger \mathbf{M}_d \mathbf{D}_R = \begin{pmatrix} m_d & 0 & 0 \\ 0 & m_s & 0 \\ 0 & 0 & m_b \end{pmatrix}, \quad \mathbf{U}_L^\dagger \mathbf{M}_u \mathbf{U}_R = \begin{pmatrix} m_u & 0 & 0 \\ 0 & m_c & 0 \\ 0 & 0 & m_t \end{pmatrix}, \quad (1-26)$$

where the mass eigenvalues are real and positive. But this transformation also amounts to diagonalizing the Yukawa coupling matrices, thus revealing that the quark masses also depend on their couplings and the vacuum expectation value in the same fashion as the charged leptons.

## 1.2 The Higgs Boson

While the Standard Model predicts the existence of the Higgs boson, it does not predict the value of its self-coupling  $\lambda$  and therefore its mass  $m_H$  is an unknown parameter of the model. Theoretical constraints based on unitarity bounds, the stability of the vacuum, and the energy scale of Standard Model physics only place the value of  $m_H$  within a wide range from 100 GeV up to 1 TeV. Stronger limits on  $m_H$ , not to mention an observation of the elusive boson, would have to be obtained from experimental results. During the 1980s, experimental searches for the Higgs boson began in earnest as particle accelerators finally reached energies that enabled the predicted mass range to be studied. The current era of high-energy physics experiment is now dominated by experiments at the Large Hadron Collider (LHC) and so the following qualitative review of Standard Model Higgs boson phenomenology is framed in its context.

### 1.2.1 Phenomenology

The Standard Model Higgs boson is predicted to be a spinless particle with zero electric or color charge that is even under the combined symmetry of charge conjugation and parity (CP-symmetry). It is also predicted to couple to the gauge bosons, fermions, and itself<sup>7</sup> in proportion to their masses according to

$$\begin{aligned} g_{Hf\bar{f}} &= \frac{m_f}{v}, & g_{HVV} &= \frac{2m_V^2}{v}, & g_{HHVV} &= \frac{2m_V^2}{v^2}, \\ g_{HHH} &= \frac{3m_H^2}{v}, & g_{HHHH} &= \frac{3m_H^2}{v^2}, \end{aligned} \tag{1-27}$$

where  $V = W$  or  $Z$  and  $v$  is the vacuum expectation value.<sup>[11]</sup> These interactions may be expressed as the Feynman diagram vertices shown in Figure 1-3. Because the Higgs boson might be coaxed into existence by these interactions, the production modes of the Higgs boson have informed the development of modern hadron colliders. By the same token,

---

<sup>7</sup> The Higgs self-couplings come from the higher order terms of Equation 1-6.

those interactions provide the means for the massive Higgs boson to decay into lighter and more stable particles. The decay modes of the Higgs boson thus influence the design of particle detectors capable of accurately measuring the properties of its decays products.

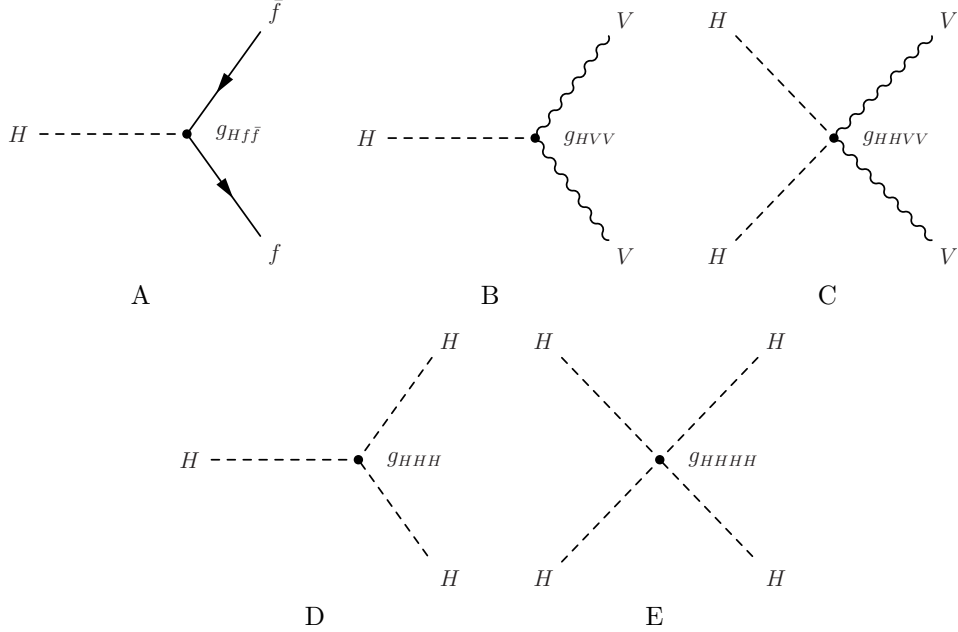


Figure 1-3. The Feynman diagrams for the vertices of the Standard Model Higgs boson representing the A) fermion-Higgs interaction; B) trilinear gauge-Higgs interaction; C) quartic gauge-Higgs interaction; D) trilinear self-interaction; E) quartic self-interaction.

### 1.2.1.1 Production modes

The production of massive particles such as the Higgs boson proceeds from the interactions of hadrons made to collide at high energies. The probability that such a collision results in a specific interaction is known as a cross section  $\sigma$ . The production cross sections of the Higgs boson depend on the center-of-mass energy of the collision  $\sqrt{s}$  and its mass  $m_H$ , and have been determined by theoretical calculations to behave as shown in Figure 1-4.

The dominant production mode is gluon fusion ( $pp \rightarrow H$ ), in which a gluon from each of the colliding hadrons form a virtual quark loop. Because the Higgs boson couples to quarks in proportion to their masses, it can be radiated from the resulting virtual

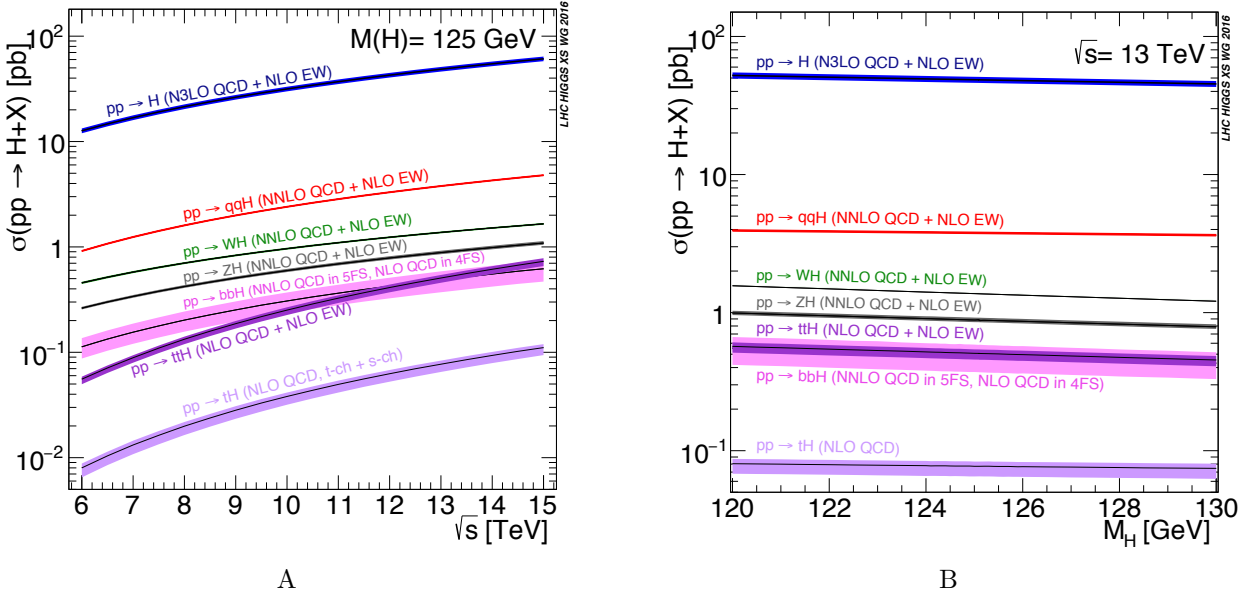


Figure 1-4. The production cross section for the Higgs boson as A) a function of the center of mass energy  $\sqrt{s}$  for  $m_H = 125 \text{ GeV}$ ; B) a function of  $m_H$  for  $\sqrt{s} = 13 \text{ TeV}$ . The shaded bands show the combined parametric and theoretical uncertainties and the labels indicate the production mode and any radiative corrections considered.[13]

top quark or, to a lesser extent, bottom quark loop. The production mode with the second-largest cross section is vector boson fusion ( $pp \rightarrow q\bar{q}H$ ), which proceeds from the parton scattering of two quarks, or anti-quarks, via their exchange of weak vector bosons  $V$ . This produces a Higgs boson because of the allowed trilinear gauge-Higgs interaction. The vector boson associated production mode ( $pp \rightarrow VH$ ), or *Higgstrahlung*, has the third-largest cross section. This production mechanism proceeds from the weak interaction of a quark and an anti-quark from which a Higgs boson is radiated by the virtual  $W$  or  $Z$  weak vector boson. Because the  $Z$  associated production can also be induced via a virtual top quark loop, contributions of nearly 15% to the total production cross section of this mode come from the process  $gg \rightarrow ZH$ . The fourth relevant production mode is top quark pair associated production ( $pp \rightarrow t\bar{t}H$ ). Rather than forming a virtual top quark loop, a gluon from each of the colliding hadrons decays into a top quark-antiquark pair and a Higgs boson is produced by the annihilation of a top quark of one pair and the

top anti-quark of the other. The smallest cross sections are contributed by the single top quark associated production and bottom quark pair associated production modes, which are suppressed relative to the main production modes. The Feynman diagrams for the main production modes are shown in Figure 1-5.

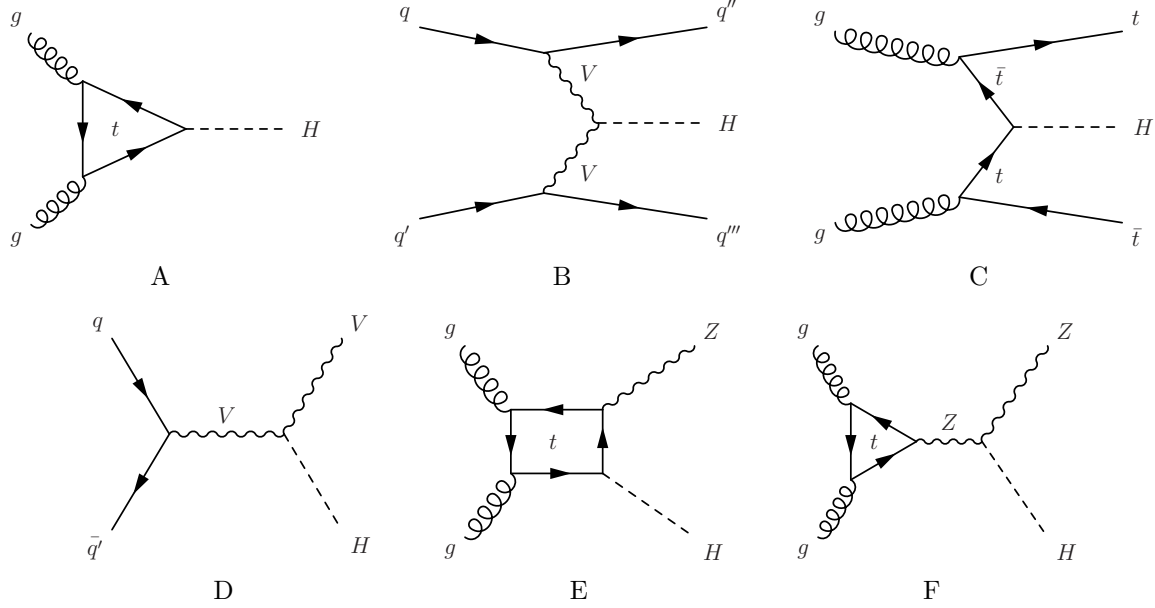


Figure 1-5. The Feynman diagrams for the Higgs boson production processes of A) gluon fusion; B) vector boson fusion; C) top quark pair associated production; D) vector boson associated production; E), F) top-loop induced contributions to the  $Z$  boson associated production.

For the current center-of-mass energy of proton collisions at the LHC,  $\sqrt{s} = 13$  TeV, and a Higgs boson mass of  $m_H = 125$  GeV, the state-of-the-art values computed for the production cross sections<sup>8</sup> are

$$\sigma(pp \rightarrow H) = 48.58^{+4.6\%}_{-6.7\%} \text{ (theory)} \pm 3.2\% \text{ (PDF + } \alpha_s \text{) pb},$$

$$\sigma(pp \rightarrow qqH) = 3.782^{+0.4\%}_{-0.3\%} \text{ (QCD scale)} \pm 2.1\% \text{ (PDF + } \alpha_s \text{) pb},$$

$$\sigma(pp \rightarrow WH) = 1.373^{+0.5\%}_{-0.7\%} \text{ (QCD scale)} \pm 1.9\% \text{ (PDF + } \alpha_s \text{) pb},$$

---

<sup>8</sup> The cross sections are presented in units of picobarns (pb), where 1 barn =  $10^{-24}$  cm<sup>2</sup>.

$$\begin{aligned}\sigma_{\text{total}}(pp \rightarrow ZH) &= 0.8839^{+3.8\%}_{-3.1\%} (\text{QCD scale}) \pm 1.6\% (\text{PDF} + \alpha_s) \text{ pb}, \\ \sigma(gg \rightarrow ZH) &= 0.1227^{+25.1\%}_{-18.9\%} (\text{QCD scale}) \pm 2.4\% (\text{PDF} + \alpha_s) \text{ pb}, \\ \sigma(pp \rightarrow ttH) &= 0.5071^{+5.8\%}_{-9.2\%} (\text{QCD scale}) \pm 3.6\% (\text{PDF} + \alpha_s) \text{ pb}.\end{aligned}$$

The uncertainties are due to variations on the QCD renormalization scale (QCD scale), the parton distribution function (PDF) that determines the momenta of the interacting partons, and the strong coupling constant ( $\alpha_s$ ). The accuracy of these cross sections are determined by the inclusion of higher-order terms during their calculation, which is generally next-to-next-to-leading (NNLO) order in QCD and next-to-leading order (NLO) in electroweak corrections. The exceptions are that the gluon fusion cross section is calculated further to N3LO in QCD, hence acquiring additional theoretical uncertainties, and the top quark pair associated production cross section which is calculated only to NLO in QCD. The methods and theoretical treatment of these cross section calculations are thoroughly documented in Ref. [13].

### 1.2.1.2 Decay modes

With a predicted lifetime<sup>9</sup> of  $1.6 \times 10^{-22}$  s, the Higgs boson decays almost immediately and its presence can only be inferred from its decay products. Based on its predicted properties, the final state of its decay must be electrically and color neutral. By conservation of mass, it must also decay into lighter particles so, for example, a decay into a top quark-antiquark pair  $t\bar{t}$  is forbidden for low mass Higgs bosons. However, because the Higgs boson couples to particles in proportion to their masses, the heaviest allowed decays will be the most favored.

The probability of a particular decay mode occurring is given by its *branching ratio*, and is shown in Figure 1-6 as a function of the Higgs boson mass  $m_H$ . For a Higgs boson

---

<sup>9</sup> The total decay width of the Higgs boson is predicted to be  $\Gamma_H = 4.088$  MeV and the lifetime of a particle is given by  $\tau = \hbar / \Gamma$ .

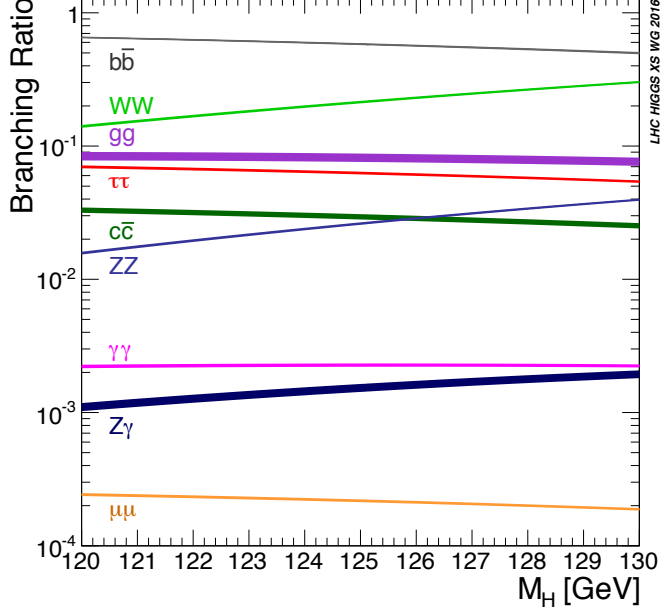


Figure 1-6. The branching ratios of the Higgs boson as a function of its mass  $m_H$ . [13].  
The shaded bands indicate the theoretical uncertainty of the calculation while the labels indicate the decay mode.

mass of  $m_H = 125$  GeV, the state-of-the-art values computed for the branching ratios of its allowed decays are, in descending order,

$$\begin{aligned}
\text{BR}(H \rightarrow b\bar{b}) &= 0.5824^{+0.65\%}_{-0.65\%} (\text{theory})^{+0.72\%}_{-0.74\%} (m_q)^{+0.78\%}_{-0.80\%} (\alpha_s), \\
\text{BR}(H \rightarrow WW) &= 0.2137^{+0.99\%}_{-0.99\%} (\text{theory})^{+0.99\%}_{-0.98\%} (m_q)^{+0.66\%}_{-0.63\%} (\alpha_s), \\
\text{BR}(H \rightarrow gg) &= 0.08187^{+3.40\%}_{-3.41\%} (\text{theory})^{+1.12\%}_{-1.13\%} (m_q)^{+3.69\%}_{-3.61\%} (\alpha_s), \\
\text{BR}(H \rightarrow \tau\bar{\tau}) &= 0.06272^{+1.17\%}_{-1.16\%} (\text{theory})^{+0.98\%}_{-0.98\%} (m_q)^{+0.62\%}_{-0.62\%} (\alpha_s), \\
\text{BR}(H \rightarrow c\bar{c}) &= 0.02891^{+1.20\%}_{-1.20\%} (\text{theory})^{+5.26\%}_{-0.98\%} (m_q)^{+1.25\%}_{-1.25\%} (\alpha_s), \\
\text{BR}(H \rightarrow ZZ) &= 0.02619^{+0.99\%}_{-0.99\%} (\text{theory})^{+0.99\%}_{-0.98\%} (m_q)^{+0.66\%}_{-0.63\%} (\alpha_s), \\
\text{BR}(H \rightarrow \gamma\gamma) &= 0.002270^{+1.73\%}_{-1.72\%} (\text{theory})^{+0.93\%}_{-0.99\%} (m_q)^{+0.61\%}_{-0.62\%} (\alpha_s), \\
\text{BR}(H \rightarrow Z\gamma) &= 0.001533^{+5.71\%}_{-5.71\%} (\text{theory})^{+0.98\%}_{-1.01\%} (m_q)^{+0.58\%}_{-0.65\%} (\alpha_s), \\
\text{BR}(H \rightarrow \mu\bar{\mu}) &= 0.0002176^{+1.23\%}_{-1.23\%} (\text{theory})^{+0.97\%}_{-0.99\%} (m_q)^{+0.59\%}_{-0.64\%} (\alpha_s).
\end{aligned}$$

The theoretical uncertainties account for missing higher-order QCD and electroweak corrections, while the parametric uncertainties cover the variations of the quark masses  $m_q$ , where  $q = c, b, t$ , and the strong coupling constant  $\alpha_s$  which are input parameters to the calculation. The methods and theoretical treatment of the computation of these branching ratios is also documented in Ref. [13].

### 1.2.2 Discovery

The discovery of a new boson with a mass close to 125 GeV was announced on July 4, 2012 at CERN, with independent observations achieved by the ATLAS[14] and CMS[15] collaborations. Within a year’s time, the new particle would be verified by both experiments to have zero spin and positive parity[16, 17] and its observed couplings would remain consistent with a Standard Model Higgs boson.[18] At this point, the new boson was recognized as a Higgs boson, and in 2013 the Nobel Prize in Physics would be awarded to François Englert and Peter Higgs for their discovery of the Higgs mechanism and prediction of a Higgs boson almost half a century before its discovery.

The decay channels with the highest sensitivities were  $H \rightarrow ZZ$ , with each  $Z$  boson subsequently decaying into a pair of charged leptons, and  $H \rightarrow \gamma\gamma$ , for which ATLAS and CMS both had observed local significances above the expected background of  $3\sigma$  and  $4\sigma$ , respectively. While those channels individually passed the  $3\sigma$  threshold for establishing evidence, it would take their combination with other channels for ATLAS to surpass and CMS to reach  $5\sigma$ , the threshold for declaring a discovery. By the beginning of 2015, when the LHC would resume operations since its first planned maintainence period, the Higgs production modes of gluon fusion and vector boson fusion had been observed, as well as its decays to  $WW$ ,  $ZZ$ , and  $\gamma\gamma$ .

## 1.3 Searches for $VH(b\bar{b})$

The preferred decay mode of the Higgs boson, as determined by its measured mass of  $m_H = 125.26 \pm 0.16$  GeV[11], is to a bottom quark-antiquark pair, henceforth  $H(b\bar{b})$ , with a branching ratio of nearly 59%. An observation would establish clearly the coupling

of the Higgs boson to bottom quarks, and to down-type quarks in general. Moreover, as the dominant decay mode, a precise measurement of its branching ratio has direct ramifications for improving the constraints on the total decay width of the Higgs boson and provides an opportunity to check for anomalous Yukawa couplings that may present a case for new physics beyond the Standard Model. The observation of  $H(b\bar{b})$  is therefore of great scientific interest and experiments must be dedicated towards searching for this decay.

### 1.3.1 Motivation for $VH(b\bar{b})$

The experimental challenge of searching for  $H(b\bar{b})$  is in distinguishing its decay signature, or signal, from the immense background of Standard Model processes. The bottom and antibottom quarks produced by the decay will both hadronize due to color confinement, forming two unstable B-hadrons that subsequently decay into cones of lighter particles known as jets. Such a final state is not unique, as QCD processes which produce many jets are a common occurrence. However, even if the pair of jets can be correctly identified as originating from bottom quarks and not lighter quarks or gluons, the multijet production of a bottom quark-antiquark pair occurs at a rate that is seven orders of magnitude greater than the gluon fusion production of a Higgs boson that decays into a bottom quark-antiquark pair, as shown in Figure 1-7. While advances in the field of jet substructure may eventually enable such a strategy[19], a direct search for final states containing only two  $b$ -jets faces a large and irreducible multijet background.

One solution for mitigating the multijet background is searching for  $H(b\bar{b})$  using the remaining Higgs boson production modes and exploiting their final state topologies. The vector boson fusion final state is fully hadronic, as the two scattering quarks will form their own jets, and is challenging in its own right. The top-quark associated production final state potentially contains leptons from the dominant decay of the top quark,  $t \rightarrow Wb$ , but a combinatorial complexity arises with the presence of additional  $b$ -jets. The key lies in using the weak vector boson associated production mode, henceforth  $VH(b\bar{b})$ , which

offers a final state that can be distinguished by the leptonic decays of either the  $W$  or  $Z$ , thereby enabling the reduction of the multijet background to negligible levels.

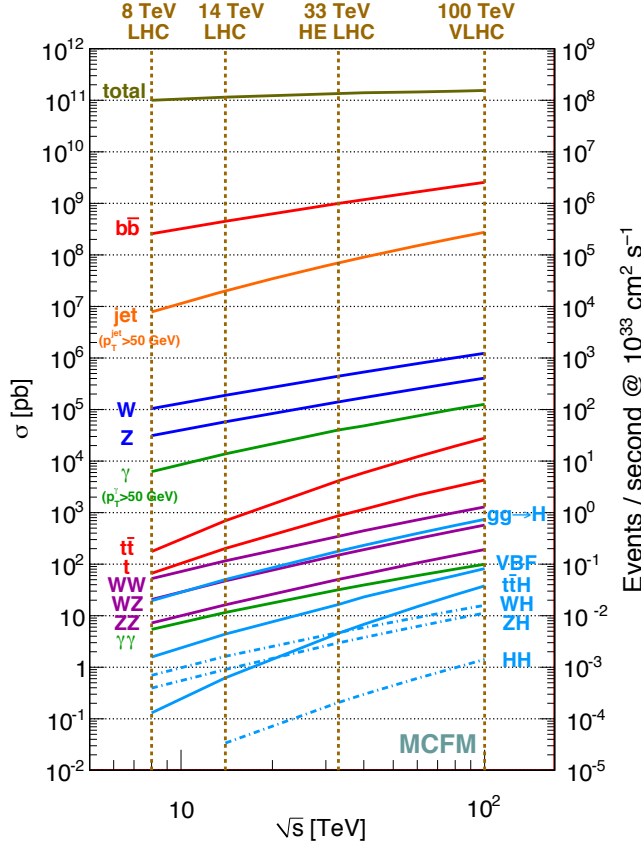


Figure 1-7. The predicted production cross sections of various processes for the range of center-of-mass energies achieved and within reach at the LHC.[20]

Searches based on  $VH(b\bar{b})$  must also contend with known Standard Model background processes, such as those measured in Figure 1-8, which mimic its final states. The main irreducible backgrounds come from  $W$  and  $Z$  bosons produced in association with jets, or  $V + \text{jets}$ , and the production of top quark-antiquark pairs, or  $t\bar{t}$ , which have cross sections that are three to four orders of magnitude larger than that of  $VH(b\bar{b})$ . The single top and diboson, or  $VV$ , processes are also important backgrounds, but with cross sections that are only one to two orders of magnitude larger than that of  $VH(b\bar{b})$ . The Feynman diagrams for examples of these background processes are shown in Figure 1-9.

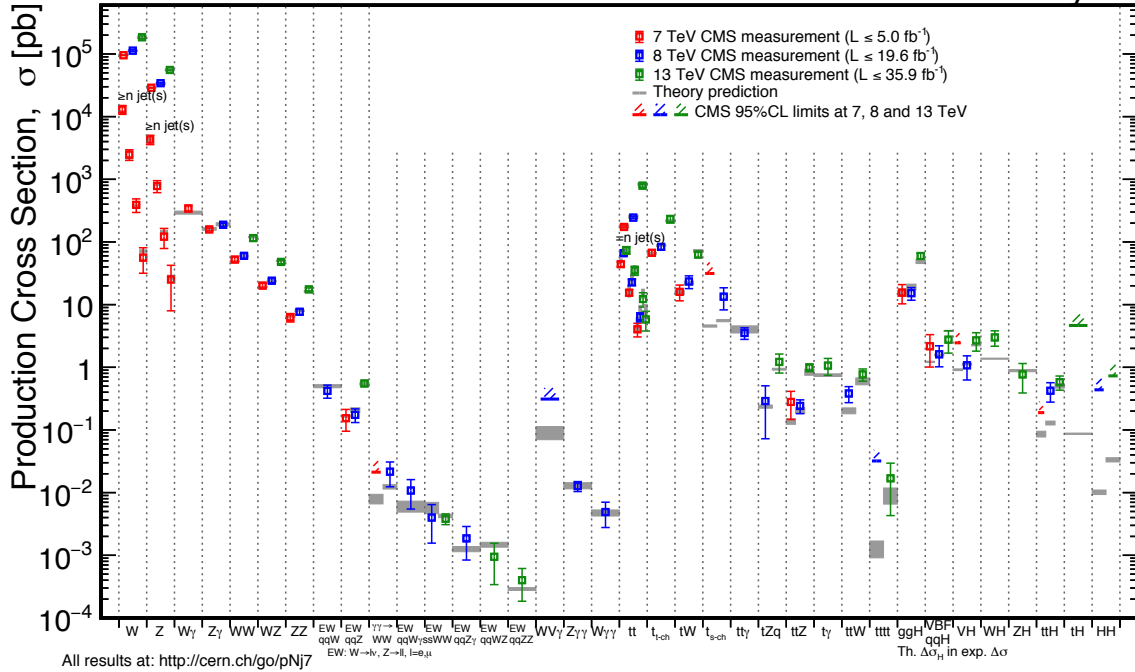


Figure 1-8. Measurements of the production cross sections of the Standard Model processes by the CMS experiment.[21]. The agreement with prediction holds remarkably well across the different center-of-mass energies of collisions at the LHC.

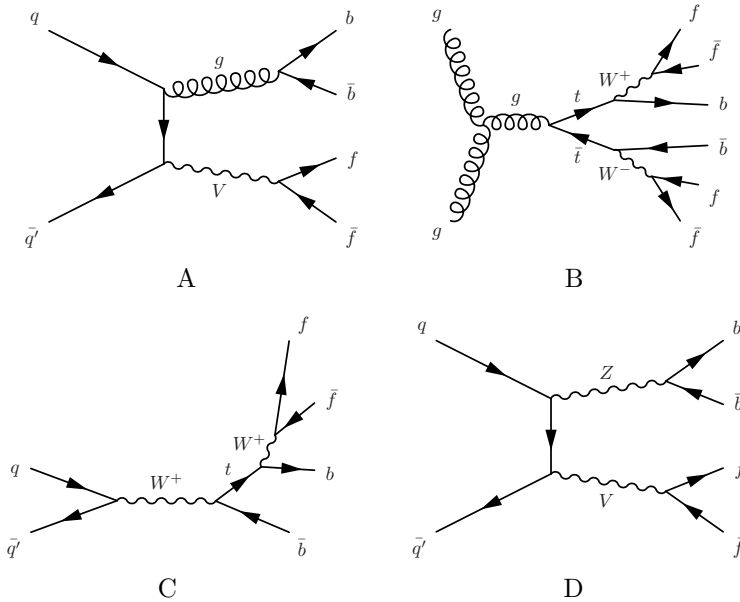


Figure 1-9. The Feynman diagrams for the Standard Model background processes to  $VH(b\bar{b})$ . A) vector boson production in association with jets ( $V + \text{jets}$ ); B) top quark-antiquark pair production ( $t\bar{t}$ ); C) single top D) diboson ( $VV$ ).

### 1.3.2 Previous Results

The first searches for  $VH(b\bar{b})$  coincided with the first searches for the Higgs boson and began at the Large Electron-Positron (LEP) collider which operated from 1989 to 2000 at CERN in Geneva, Switzerland. At LEP, a Higgs boson would have been produced primarily through  $Z$  boson associated production initiated by the annihilation of an electron-positron pair. Although the Higgs boson was not found, the four LEP experiments ALEPH, DELPHI, OPAL, and L3 analyzed the full dataset collected at center-of-mass energies above  $\sqrt{s} = 189$  GeV and established a lower bound of 114.4 GeV for the mass of the Higgs boson at the 95% confidence level.[22]

The first searches for  $VH(b\bar{b})$  using hadron collisions were done at the Tevatron at Fermi National Accelerator Laboratory (FNAL) in Batavia, Illinois. The Tevatron collided protons and antiprotons at center-of-mass energies up to  $\sqrt{s} = 1.96$  TeV and operated from 1985 until 2011. Although the Higgs boson was not observed, a combined analysis of the full Tevatron datasets collected by the CDF and D0 experiments yielded an observed significance of  $2.8\sigma$ , just shy of establishing evidence for the  $VH(b\bar{b})$  decay.[23]

The most recent searches for  $VH(b\bar{b})$  have taken place at the Large Hadron Collider (LHC), also located at CERN, using collisions between protons. During Run 1, which lasted from 2010 to 2013, the LHC collided protons at center-of-mass energies of  $\sqrt{s} = 7$  and 8 TeV. Analysis of the Run 1 datasets were unable to obtain evidence for  $VH(b\bar{b})$  with observed significances of  $1.4\sigma$  and  $2.5\sigma$  by the ATLAS and CMS experiments, respectively.[24, 25] A combination of these results only brought the observed significance up to  $2.6\sigma$ .[26]

After its upgrades during Long Shutdown 1 (LS1), the LHC resumed operations and Run 2 commenced with the center-of-mass energy of collisions increased to  $\sqrt{s} = 13$  TeV. Although the increase in energy meant a larger cross section for  $VH(b\bar{b})$ , it also led to relatively larger increases in the cross sections of the Standard Model background processes as demonstrated in Table 1-1, further complicating the search for  $VH(b\bar{b})$ .

However, this pessimism was unwarranted, as ATLAS and CMS both established evidence for the  $VH(b\bar{b})$  decay by observing significances of  $3.6\sigma$  and  $3.8\sigma$ , respectively, after combining the results of their initial Run 2 and Run 1 analyses.[\[27, 28\]](#)

Table 1-1. A list of Higgs boson and Standard Model background production cross sections at center-of-mass energies of  $\sqrt{s} = 8$  and 13 TeV, along with the relative increase at  $\sqrt{s} = 13$  TeV.

Cross Section	$\sqrt{s} = 8$ TeV	$\sqrt{s} = 13$ TeV	Relative Increase at $\sqrt{s} = 13$ TeV
$\sigma(pp \rightarrow H)$	19.4 pb	44.1 pb	2.27
$\sigma(pp \rightarrow qqH)$	1.6 pb	3.8 pb	2.38
$\sigma(pp \rightarrow VH)$	1.23 pb	2.26 pb	1.84
$\sigma(pp \rightarrow ttH)$	133 fb	507 fb	3.81
$\sigma(pp \rightarrow t\bar{t})$	253 pb	832 pb	3.29

Naive projections assuming increased statistics and similar systematic uncertainties suggested that an observation of  $VH(b\bar{b})$  may be possible if the experimental sensitivity could be improved by about 20%. With Run 2 on track to produce more data in 2017 than 2016, such a historic result appeared to be on the horizon. The analysis of the 2017 dataset and the results obtained by the CMS experiment are the subject of this dissertation.

## CHAPTER 2

### EXPERIMENTAL APPARATUS

It is nature's irony, that the study of subatomic particles requires the largest and most intricate machines known to date in human history. Because the physics of such particles are described by their interactions, high energy physics experiments typically accelerate particles to extreme kinetic energies, collide them against each other or dense targets, and infer the details of their interaction from the resulting final state particles. Such collisions can be *elastic*, where the interacting particles merely exchange energy and remain unchanged, or *inelastic*, where the interaction changes the incoming particles and has a chance of creating new, massive particles because of the time-energy uncertainty relation. Collisions of the latter kind are thus of great interest to experimentalists in the search for new particles and their decays.

Under the consideration of providing as much energy as possible towards the interaction, modern experiments favor colliding beams over fixed-target experiments. By momentum conservation, some of the energy of a fixed-target collision must be converted into the kinetic energies of final state particles, while there is no such constraint for colliding beams. Thus, at high energies, the dependence of the center-of-mass energy  $\sqrt{s}$  on the incoming beam energy  $E_{\text{beam}}$  in the laboratory frame scales as  $\sqrt{s} \propto E_{\text{beam}}^{1/2}$  for fixed-targets, whereas it scales linearly for colliding beams  $\sqrt{s} \propto E_{\text{beam}}$ . Because the center-of-mass energy of the collision fixes the energy available for the production of new particles, colliding beams hold the advantage.

Modern experiments also favor circular rather than linear particle accelerators. Because the length of a linear accelerator is correlated with its maximum beam energy, the size required to probe the current energy frontier is prohibitively large, and even then particles can only be accelerated once through the machine. Instead, circular colliders can accelerate particles for multiple orbits until they reach the desired energy scale, and this circulation also allows for the same beams to be collided multiple times to achieve

a *luminosity*, a measure of particle flux, that is higher than linear accelerators. The problem faced by circular colliders is synchrotron radiation, where charged particles accelerated along a circular trajectory lose energy. Because a particle's energy loss due to synchrotron radiation is inversely proportional to the fourth power of its mass, electron beams experience incredible energy losses compared to proton beams. For this reason, modern experiments prefer the acceleration and collision of hadron beams.

## 2.1 The Large Hadron Collider

The Large Hadron Collider (LHC) at CERN is the culmination of contemporary high energy experiment sensibilities. The world's largest machine, it is a circular accelerator with a circumference of 27 km, spanning across the Franco-Swiss border, and is housed within an underground tunnel at an average depth of 100 m. An illustration is provided in Figure 2-1. It features two parallel evacuated beam pipes in which proton beams circulate in opposite directions. Although the design energy of each proton beam is 7 TeV, the beams are currently circulating at an energy of 6.5 TeV to give a center-of-mass energy of 13 TeV for the one billion proton collisions it produces per second.

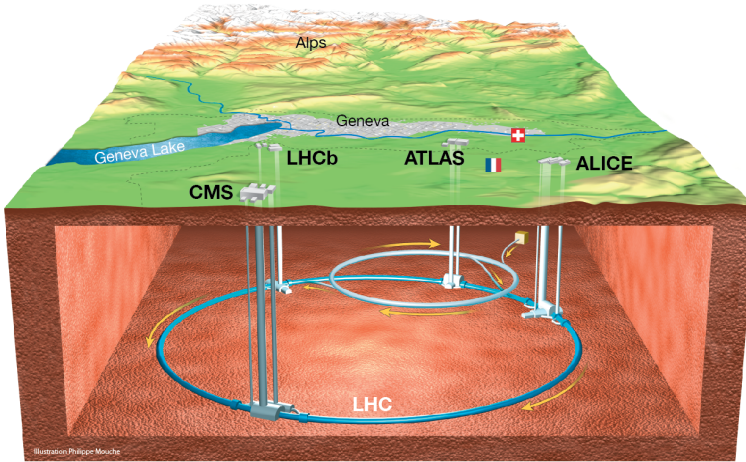


Figure 2-1. An overall view of the LHC showing the underground tunnel and its experiments in relation to its geography.[29]

Because the LHC reuses the tunnels of the Large Electron-Positron (LEP) Collider, additional excavation was avoided and it was integrated as the final stage of CERN's accelerator complex, shown in Figure 2-2. The source of protons is a canister of hydrogen gas to which a strong electric field is applied to strip the electrons from the hydrogen nuclei. The protons then pass through the linear accelerator LINAC2 and are accelerated to an energy of 50 MeV. They are then injected into successive circular accelerators: the Proton Synchrotron Booster which accelerates the beams to 1.4 GeV, the Proton Synchrotron (PS) which accelerates the beams to 25 GeV, the Super Proton Synchrotron (SPS) which further accelerates the beams to 450 GeV, and finally the LHC itself. The oscillating radio frequency (RF) fields used to accelerate the protons results in beams composed of proton *bunches* as opposed to a continuous stream. The LHC currently circulates up to 2556 bunches per beam, which is not far from its design value of 2808 bunches per beam.

The circular orbit of the proton beams are maintained by the 1,232 bending magnets lining the LHC. The bending magnets are superconducting dipole magnets which generate 8.3 T magnetic fields powerful enough to bend the high energy beams. In order to minimize the oscillation of the bunches around their trajectories and achieve high luminosity, 392 focusing magnets are also placed along the LHC ring. The focusing magnets are superconducting quadrupole magnets with a magnetic field gradient of 223 T/m. They are placed in alternating pairs to account for their nature of focusing along one direction while defocusing the orthogonal direction. Schematics for these two main types of magnets are shown in Figure 2-3. In order to maintain the superconductivity of these magnets, the cryogenic systems cool them down to a temperature of 1.9 K.

The beams are directed to cross through each other at four sites around the LHC known as interactions points. At these points, fine control of the beam is crucial because it has direct ramifications on the number of possible interactions. The interaction rate of any

## CERN's Accelerator Complex

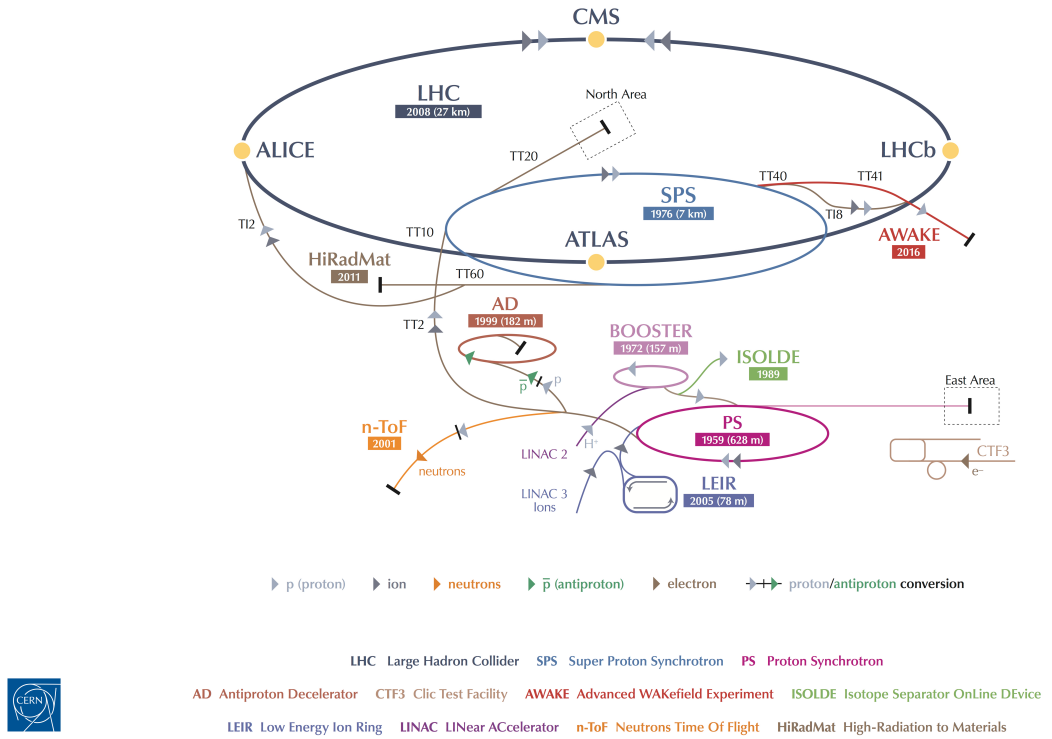


Figure 2-2. A complete schematic of the CERN acerclator complex and experiments.[30]

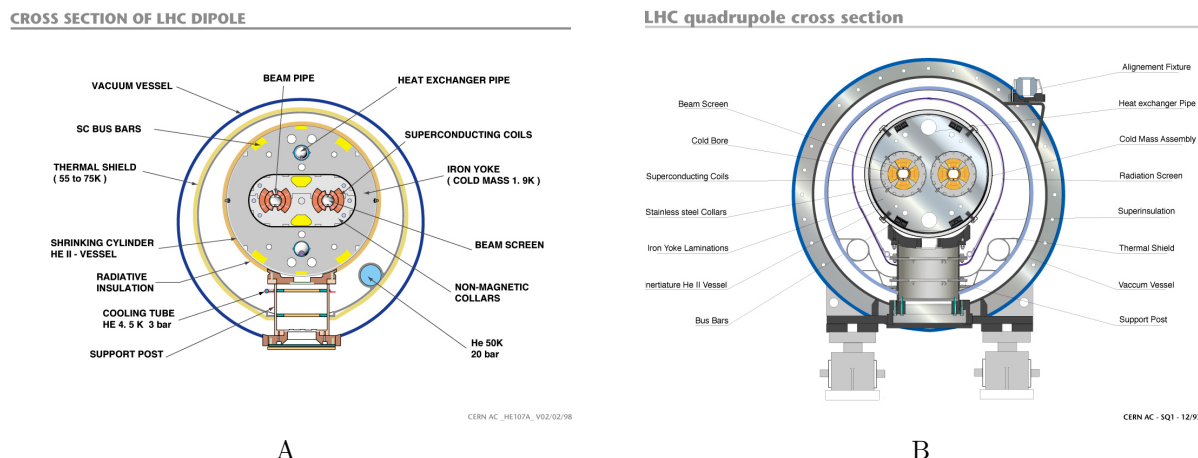


Figure 2-3. The cross sectional views for the main types of LHC magnets: A) dipole magnet used for bending the beams; B) quadrupole magnet used for focusing the beams.[31, 32]

given process is proportional to its cross section  $\sigma$  and the luminosity  $\mathcal{L}$  of the collider

$$\frac{dN}{dt} = \sigma \mathcal{L}, \quad (2-1)$$

where  $N$  refers to the number of interactions. The cross section, or interaction probability, is fixed by physics while the luminosity is determined by the collider's design, and therefore the highest possible luminosity is desired in order to observe rare interactions such as those that produce Higgs bosons. For equal, bunched beams with a rounded profile, the luminosity can be expressed as

$$\mathcal{L} = \frac{N^2 k_b f \gamma}{4\pi \epsilon_n \beta^*} F, \quad (2-2)$$

where the various parameters are determined by the design of the collider:  $N$  is the number of protons per bunch,  $k_b$  is the number of bunches,  $f$  is the revolution frequency,  $\gamma$  is the typical Lorentz factor,  $\epsilon_n$  is the normalized emittance,  $\beta^*$  is the value of the betatron function at the interaction point, and  $F$  is the geometrical reduction factor due to the crossing angle.[33]

The LHC has a 25 ns bunch spacing, or time between bunch crossings at the interaction point, which places a constraint on how large  $k_b$  and  $f$  can be. The spacing cannot be lowered due to operational safety concerns, such as providing kicker magnets enough time to ramp up and divert the bunches toward a beam dump for absorption. The normalized emittance  $\epsilon_n$  is a measure of the kinematic phase space occupied by the particles in the bunch and can be improved by reducing the size of the bunch and the spread in momentum of its particles. The beta function is a measure of the beam's transverse size and so its value at the interaction point  $\beta^*$  is determined by how well the magnets can focus the beam at the interaction point. The geometrical factor  $F$  corrects the amount by which the colliding bunches overlap as they are made to cross at a shallow angle. While a head-on collision would result in the greatest overlap, it also increases

the chances of long range electromagnetic interactions between bunches, so there is some interplay in determining the crossing angle.

Although the design luminosity of the LHC is  $10^{34} \text{ cm}^{-2}\text{s}^{-1}$ , it has exceeded expectations by achieving a luminosity of twice the designed value. As a measure of particle flux, the luminosity that has been discussed so far is a dynamic quantity and is better called *instantaneous luminosity*. The expected number of interactions  $N$  for a specific process is thus given by

$$N = \sigma \int \mathcal{L} dt = \sigma \mathcal{L}_{int}, \quad (2-3)$$

where  $\mathcal{L}_{int}$  is the *integrated luminosity*, and so the total integrated luminosity is quoted in reference to the size of particle physics datasets.

Surrounding each of the interaction points of the LHC are its four main experiments: A Large Ion Collider Experiment (ALICE), A Toroidal LHC ApparatuS (ATLAS), the Compact Muon Solenoid (CMS), and the Large Hadron Collider beauty (LHCb). Both ATLAS and CMS are general-purpose detectors designed to search for the Higgs boson and perform precise measurements of its properties, while also exploring the new energy frontier in search of physics beyond the Standard Model. The LHC can also accelerate lead ions, which is used by ALICE to study heavy-ion collisions and the dynamics of quark-gluon plasma. As general-purpose detectors, ATLAS and CMS also study heavy-ion collisions. The LHCb experiment specializes in studying the electroweak and QCD physics of heavy flavor quarks and measuring the properties of B mesons.

## 2.2 The Compact Muon Solenoid

The Compact Muon Solenoid (CMS), illustrated in Figure 2-4, is a general-purpose particle detector and one of the two main experiments at the LHC. Its cylindrical design is impressively compact for its purpose, with a diameter of 15 m and a length of 28.7 m. Although heavy, weighing in at 14,000 tonnes, the bulk of this weight comes from its steel return yoke and structural supports which together weigh 12,500 tonnes. The return

yoke guides and contains the 3.8 T magnetic field generated by the detector's namesake superconducting solenoid, which is cooled by its cryostat to a temperature of 4.5 K during operation.

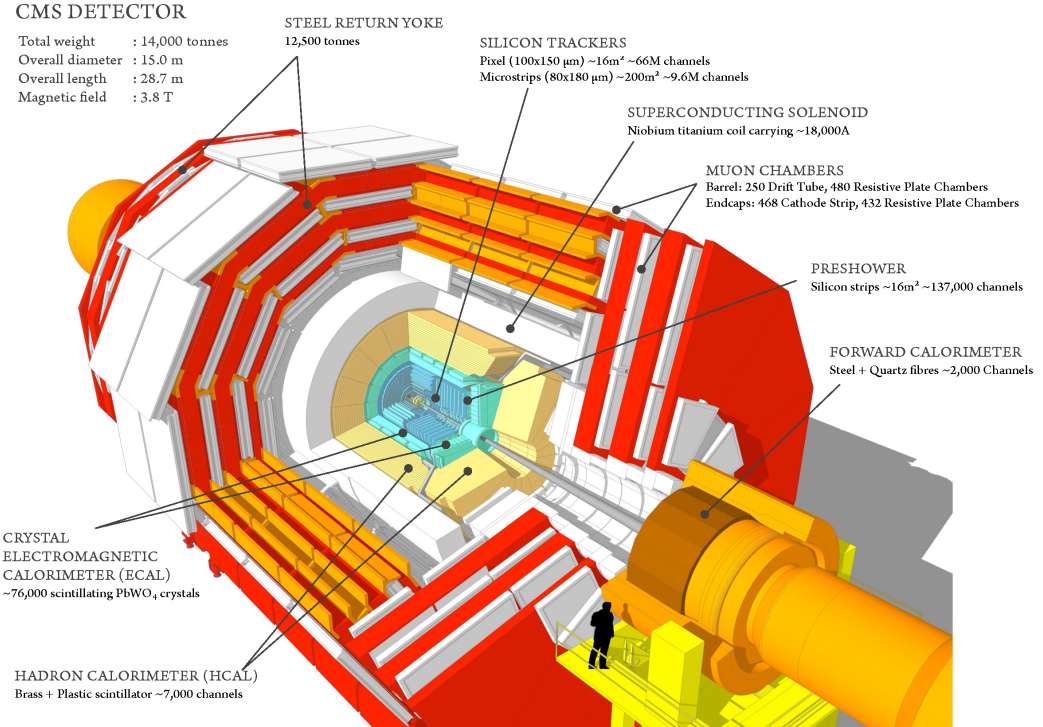


Figure 2-4. A cutaway view of the CMS detector with its main subsystems and components labeled.[34]

The solenoid is central to the design of the CMS detector because it provides a uniform magnetic field capable of bending the trajectories of charged particles as they travel through the detector, thereby enabling the measurement of their electric charge and transverse momentum  $p_T$ . This follows because a particle with electric charge  $q$  and velocity  $\mathbf{v}$  moving through a uniform magnetic field  $\mathbf{B}$  experiences a Lorentz force given by

$$\mathbf{F} = q\mathbf{v} \times \mathbf{B}. \quad (2-4)$$

Since the force is transverse to the direction of motion, the particle travels along a helical path of radius  $R$  with a handedness determined by its electric charge. An application of Newton's 2<sup>nd</sup> Law upon the circular motion of such a particle with mass  $m$  and velocity

transverse to the direction of motion  $v$  further shows that its transverse momentum is determined by the radius of curvature of its path

$$\frac{mv^2}{R} = qvB \implies p_T = qRB, \quad (2-5)$$

where  $p_T = mv$  is the transverse momentum of the particle.

While the helical paths of charged particles travelling with low momentum are fully contained within the detector, the trajectories of charged particles with high momentum are recorded as incomplete arcs, either because they decay mid-flight or, in the case of muons, travel out of the detector. While the radius of curvature of such highly energetic particles cannot be directly measured, it can be obtained by measuring the sagitta of their *track*, the arc they trace through the detector.

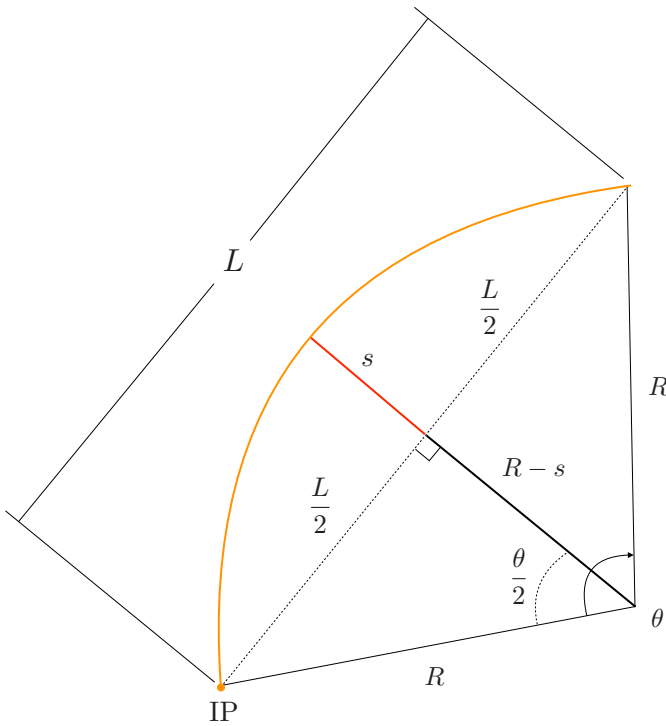


Figure 2-5. A diagram defining the sagitta of an arc representing a charged particle track (orange) travelling away from the interaction point (IP). The track has a chord of length  $L$ , an opening angle of  $\theta$ , a radius of curvature  $R$ , and a sagitta (red) of length  $s$ .

From Figure 2-5, a relationship between the chord length  $L$ , radius of curvature  $R$ , and sagitta  $s$  of the track can be constructed using the Pythagorean Theorem such that

$$R^2 = (R - s)^2 + \left(\frac{L}{2}\right)^2. \quad (2-6)$$

Solving for  $R$  with the reasonable assumption that  $s \ll L$  yields

$$R = \frac{L^2}{8s} + \frac{s}{2} \approx \frac{L^2}{8s}, \quad (2-7)$$

and therefore the  $p_T$  of a charged particle can be determined from the chord length and sagitta of its track

$$p_T = \frac{qBL^2}{8s}. \quad (2-8)$$

The magnetic field strength  $B$  and, in part, the chord length  $L$  are dictated by the design of the detector, and so the  $p_T$  resolution is limited by the resolution of the sagitta. As their momentum increases, charged particles leave straighter tracks which make it difficult to accurately measure the sagitta, thereby degrading the resolution at high momentum.

The magnetic field within the solenoid is oriented along the direction of the beam which motivates the coordinate system adopted for the CMS detector that is shown in Figure 2-6. The geometrical center of the detector defines the origin of the right-handed Cartesian coordinate system with the  $z$ -axis oriented along the direction of the anticlockwise proton beam from the LHC, the  $x$ -axis pointing horizontally towards the center of the LHC ring, and the  $y$ -axis pointing vertically upwards out of the plane of the LHC ring. The shape of the detector also admits a cylindrical description about the same origin. With the  $x$ -axis and  $z$ -axis taken to be the polar and longitudinal axes, respectively, a cylindrical coordinate system can be defined with the azimuthal angle  $\phi$  taken with respect to the positive  $x$ -axis ( $\phi = 0$ ) and the polar angle  $\theta$  taken with respect to the positive  $z$ -axis ( $\theta = 0$ ). Because the polar angle  $\theta$  is not Lorentz invariant under

boosts along the direction of the beam, it is typically transformed into the *pseudorapidity*

$$\eta = -\ln \left[ \tan \left( \frac{\theta}{2} \right) \right] \quad (2-9)$$

such that the positive  $z$ -axis has  $\eta = +\infty$  and the positive  $y$ -axis has  $\eta = 0$ .

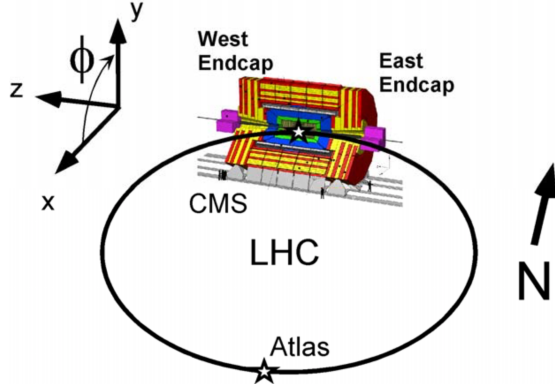


Figure 1. Overall CMS coordinate system

Figure 2-6. The conventional coordinate system of the CMS detector.[\[35\]](#)

### 2.2.1 Detector Subsystems

The CMS detector is composed of layers of subsystems dedicated towards the detection and measurement of different types of particles. Hermetic design, but fiducial volume? coverage? high pseudorapidity or very *forward* particles lost down the beam pipe or lack of coverage, radiation

A full review of the detector [\[33\]](#)

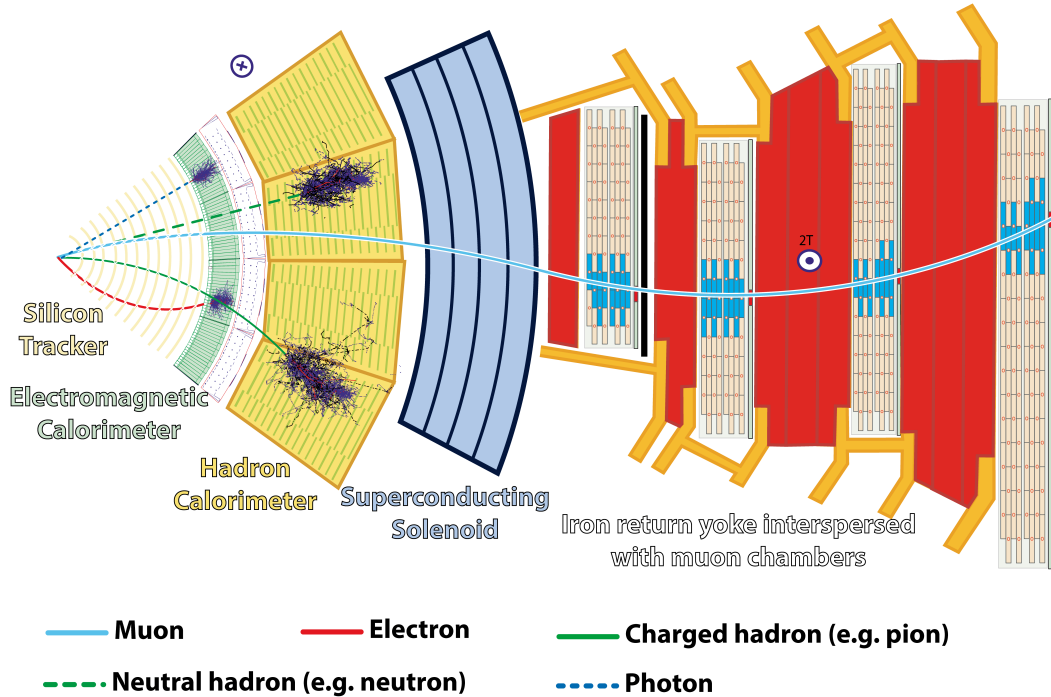


Figure 2-7. A cross sectional view of the CMS detector highlighting the different subsystems and the particles they are used to detect.[36]

### 2.2.1.1 Silicon Tracker

### 2.2.1.2 Electromagnetic Calorimeter

### 2.2.1.3 Hadronic Calorimeter

### 2.2.1.4 The Muon Subsystems

## 2.2 Data Acquisition and Triggers

### 2.2.2.1 Level 1 trigger

### 2.2.2.2 High level trigger

## 2.2.3 Computing

### 2.2.4 Upgrades for Run 2

## CHAPTER 3

### ANALYSIS STRATEGY

The first search for  $VH(b\bar{b})$  conducted by the CMS collaboration in 2012[37] demonstrated the channel’s feasibility and the overall strategy that it pioneered has remained largely intact, even through the transition to LHC Run 2. The search for  $VH(b\bar{b})$  using the 2016 dataset would establish evidence for the  $H(b\bar{b})$  decay in 2017[28] with only incremental improvements. The search for  $VH(b\bar{b})$  using the 2017 dataset would build on the physics insights and experiences obtained the year prior while bringing to bear additional event reconstruction techniques and deep learning to finally observe the  $H(b\bar{b})$  decay in 2018.[38] This chapter describes the analysis strategy used by CMS to achieve its state of the art result.

### **3.1 Data and Simulation**

#### **3.1.1 Residual Monte-Carlo Corrections**

#### **3.2 Vector Boson Reconstruction**

#### **3.3 Higgs Boson Reconstruction**

#### **3.4 Event Selection**

##### **3.4.1 Signal Regions**

##### **3.4.2 Background Control Regions**

#### **3.5 Binned Multivariate Shape Analysis**

##### **3.5.1 Input Features**

##### **3.5.2 Model Training**

##### **3.5.3 Model Selection**

##### **3.5.4 Binned Shape Analysis**

#### **3.6 Systematic Uncertainties**

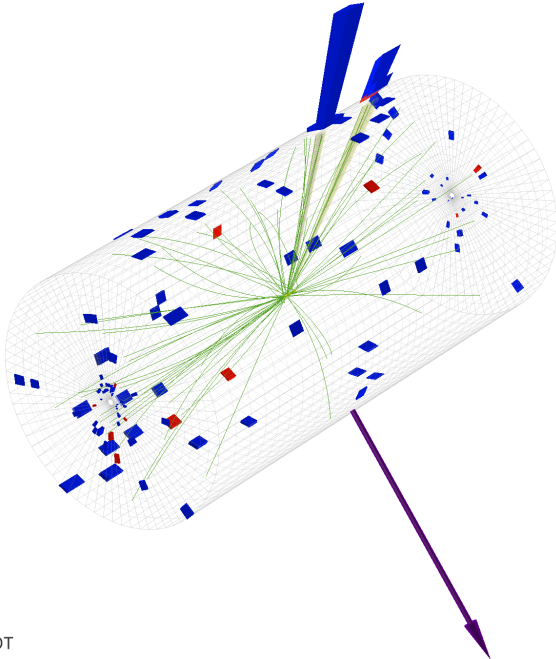
## APPENDIX A EVENT DISPLAYS

Collision events recorded by the CMS detector can be visualized as event displays using the Fireworks application developed by the CMS collaboration.[39] Event displays are used to visually summarize particle interactions with the detector’s subsystems by rendering reconstructed objects of interest such as particle tracks and jets over a 3D model of the detector. Figures A-1 through A-5 each show multiple different perspectives of an event display for a candidate signal region event from each decay channel. The candidate events were chosen based on their high DNN scores, which indicate that the DNN of their corresponding decay channel classified them as a signal event with high confidence. Although the event metadata are provided on the event displays, other event-level quantities of interest are shown in Table A-1.

Table A-1. Information for the candidate signal region events visualized by the event display. The values of the kinematic quantities are reported in units of GeV and the  $b$ -tag algorithm is DeepCSV.

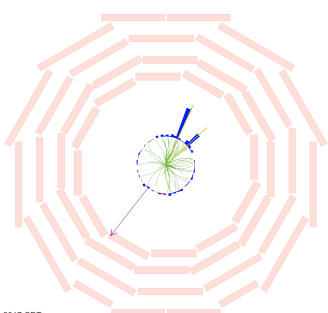
Channel	$m(jj)$	$p_T(jj)$	$p_T(j)_{\max}$	$p_T(j)_{\min}$	$b$ -tag <sub>max</sub>	$b$ -tag <sub>min</sub>	$p_T(V)$	DNN score
$Z(\nu\bar{\nu})$	121.56	319.43	195.99	129.81	0.999	0.993	319.10	0.975
$W(e\nu)$	126.49	259.66	179.31	87.31	0.999	0.995	295.75	0.989
$W(\mu\nu)$	117.69	250.55	177.33	85.28	0.996	0.995	259.80	0.993
$Z(e\bar{e})$	114.14	286.17	216.54	97.82	0.990	0.957	311.33	1.00
$Z(\mu\bar{\mu})$	111.39	100.12	78.66	69.53	0.984	0.975	466.83	1.00

For each figure, the perspective of the largest subfigure is a projection of the event display onto the  $xz$ -plane, unless otherwise specified. The perspective of both of the smaller subfigures is a projection of the event display onto the  $xy$ -plane, with the subfigure on the right zoomed in on the interaction point. This level of zoom is necessary to show the secondary vertices and their associated tracks, shown in black, and to appreciate that those tracks do not extrapolate well to any of the primary vertices, shown in yellow.



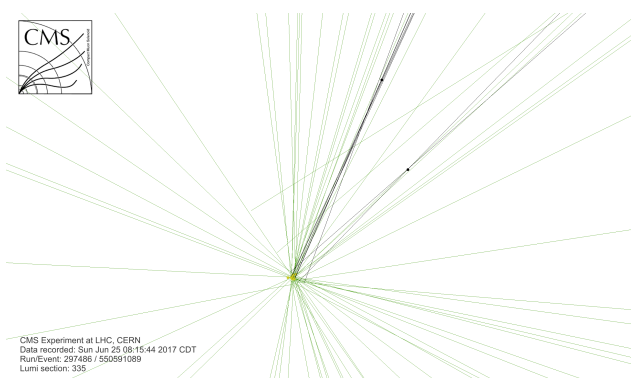
CMS Experiment at LHC, CERN  
Data recorded: Sun Jun 25 08:15:44 2017 CDT  
Run/Event: 297486 / 550591089  
Lumi section: 335

A



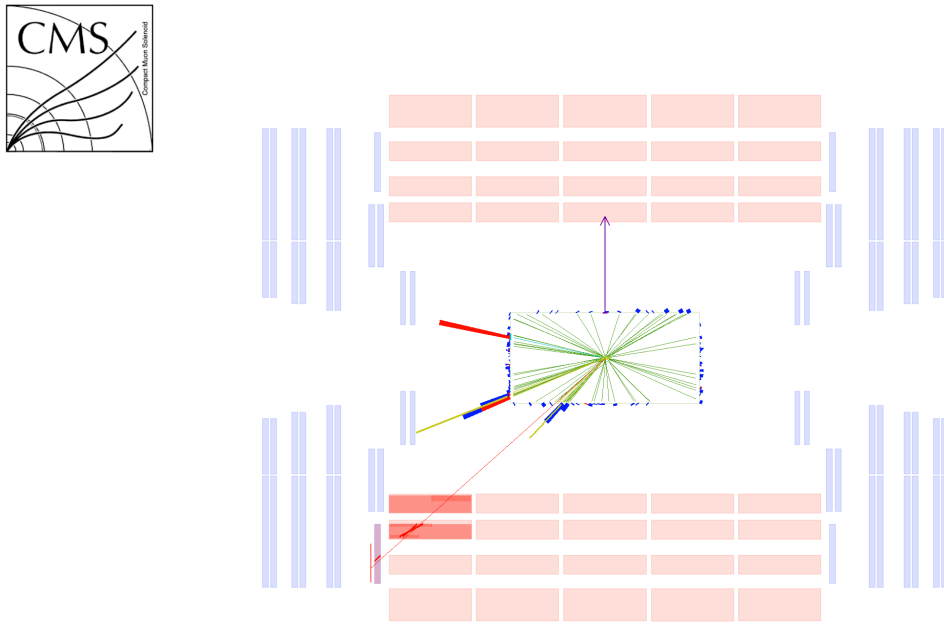
CMS Experiment at LHC, CERN  
Data recorded: Sun Jun 25 08:15:44 2017 CDT  
Run/Event: 297486 / 550591089  
Lumi section: 335

B



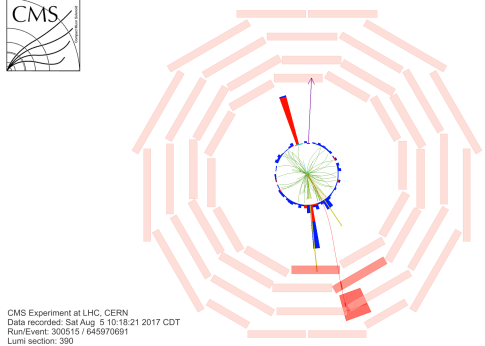
C

Figure A-1. The event display for a candidate  $Z(\nu\bar{\nu})H(b\bar{b})$  event A) from a 3D perspective view; B) projected onto the  $xy$ -plane; and C) projected onto the  $xy$ -plane and zoomed in on the interaction point. The purple arrow represents the missing transverse momentum from the invisible leptonic decay of the  $Z$  boson while the two yellow cones with their blue and red calorimeter towers represent the two  $b$ -jets from the decay of the Higgs boson. The secondary vertices of the  $b$ -jets and their associated tracks (black) are visible in C.



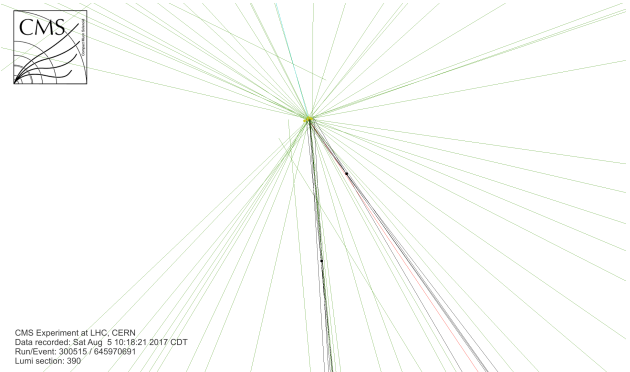
CMS Experiment at LHC, CERN  
Data recorded: Sat Aug 5 10:18:21 2017 CDT  
Run/Event: 300515 / 645970691  
Lumi section: 390

A



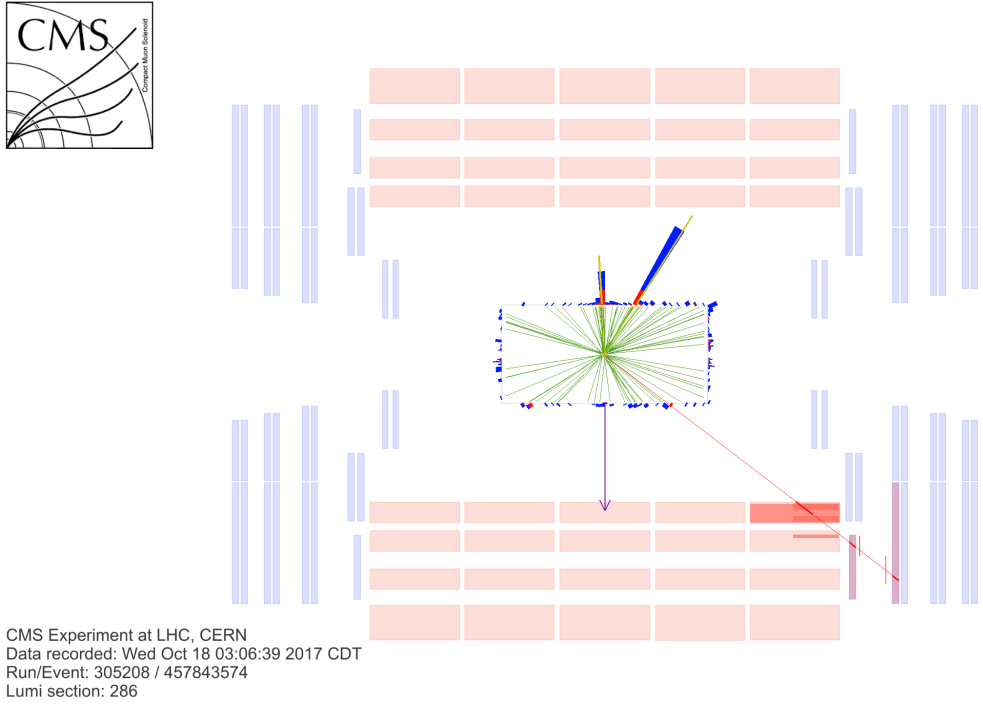
CMS Experiment at LHC, CERN  
Data recorded: Sat Aug 5 10:18:21 2017 CDT  
Run/Event: 300515 / 645970691  
Lumi section: 390

B

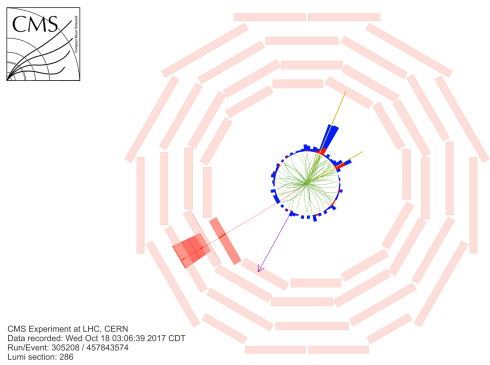


C

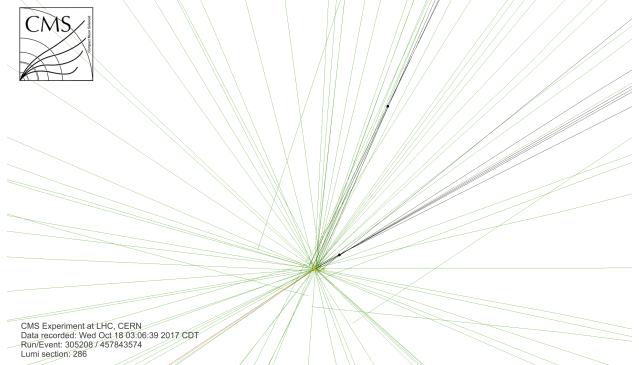
Figure A-2. The event display for a candidate  $W(e\nu)H(b\bar{b})$  event A) projected onto the  $xz$ -plane; B) projected onto the  $xy$ -plane; and C) projected onto the  $xy$ -plane and zoomed in on the interaction point. The cyan track leading to a red calorimeter tower and the purple arrow represent the electron and the missing transverse momentum from the leptonic decay of the  $W$  boson, respectively, while the two yellow cones with their blue and red calorimeter towers represent the two  $b$ -jets from the decay of the Higgs boson. The secondary vertices of the  $b$ -jets and their associated tracks (black) are visible in C. The red track associated with one of the  $b$ -jets is likely a muon resulting from a semi-leptonic decay of the  $b$ -hadron.



A



B



C

Figure A-3. The event display for a candidate  $W(\mu\nu)H(b\bar{b})$  event A) projected onto the  $xz$ -plane; B) projected onto the  $xy$ -plane; and C) projected onto the  $xy$ -plane and zoomed onto the interaction point. The red track and the purple arrow represent the muon and the missing transverse momentum from the leptonic decay of the  $W$  boson, respectively, while the two yellow cones with their blue and red calorimeter towers represent the two  $b$ -jets from the decay of the Higgs boson. The secondary vertices of the  $b$ -jets and their associated tracks (black) are visible in C.

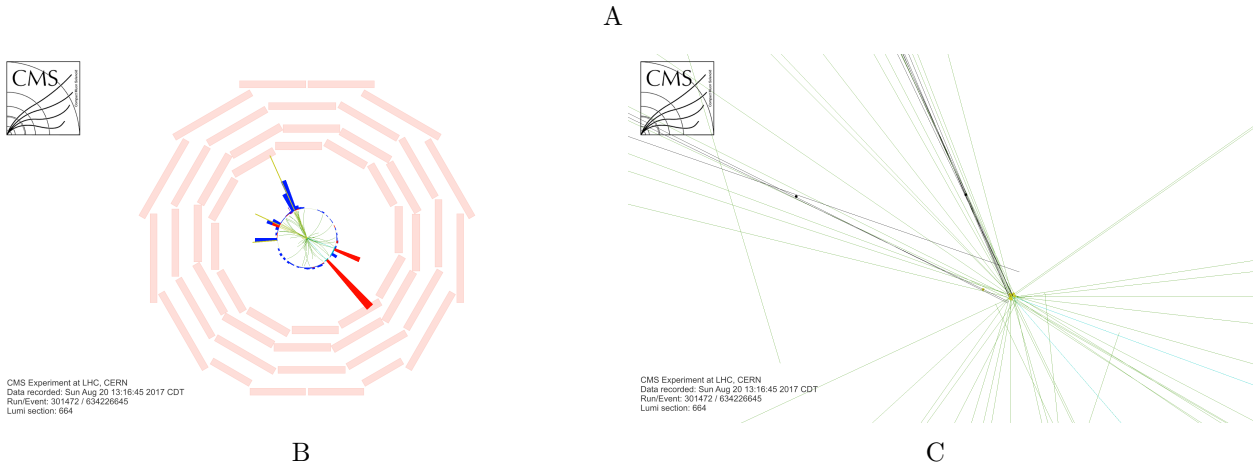
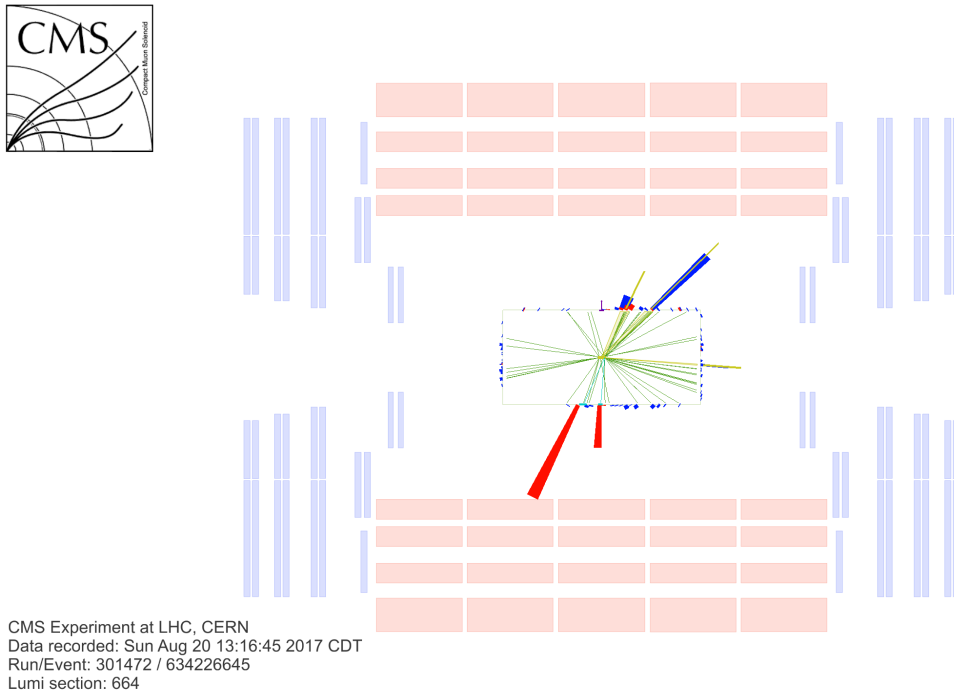


Figure A-4. The event display for a candidate  $Z(e\bar{e})H(b\bar{b})$  event A) projected onto the  $xz$ -plane; B) projected onto the  $xy$ -plane; and C) projected onto the  $xy$ -plane and zoomed onto the interaction point. The cyan tracks leading to red calorimeter towers represent the electrons from the leptonic decay of the  $Z$  boson, while the two yellow cones with their blue and red calorimeter towers represent the two  $b$ -jets from the decay of the Higgs boson. The secondary vertices of the  $b$ -jets and their associated tracks (black) are visible in C. The low missing transverse momentum close in azimuthal angle to one of the  $b$ -jets is suggestive of jet energy mismeasurement. This may be related to the blue calorimeter tower without obvious associated tracks, which may have resulted from the decay of a neutral hadron.

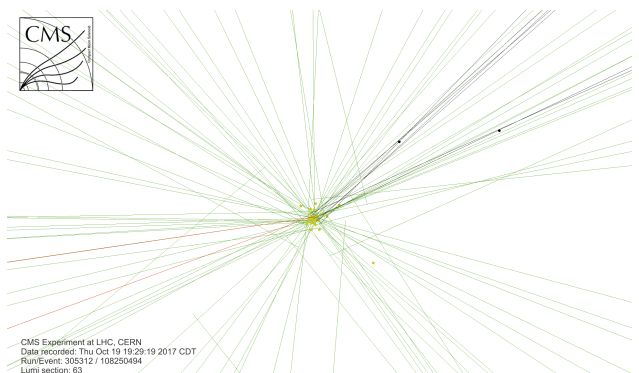
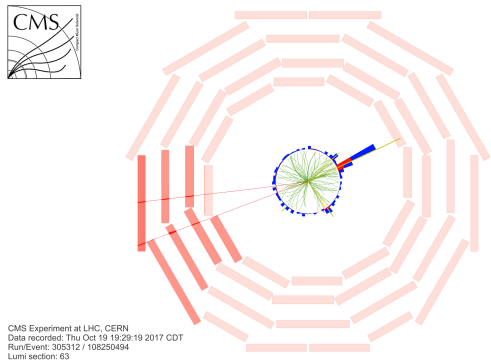
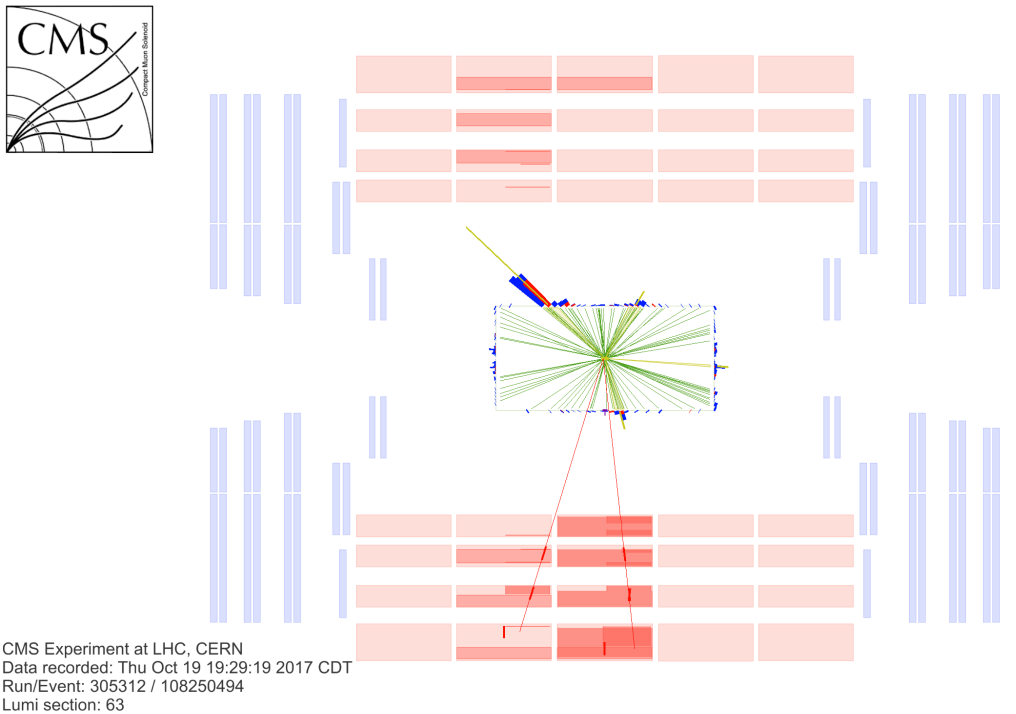


Figure A-5. The event display for a candidate  $Z(\mu\bar{\mu})H(b\bar{b})$  event A) projected onto the  $xz$ -plane; B) projected onto the  $xy$ -plane; and C) projected onto the  $xy$ -plane and zoomed onto the interaction point. The red tracks represent the muons from the leptonic decay of the  $Z$  boson, while the two yellow cones with their blue and red calorimeter towers located opposite to the red tracks represent the two  $b$ -jets from the decay of the Higgs boson. The secondary vertices of the  $b$ -jets and their associated tracks (black) are visible in C. The two other yellow cones could represent jets caused by initial or final state radiation, neither of which were  $b$ -tagged.

## REFERENCES

- [1] M. E. Peskin and D. V. Schroeder, *An Introduction to Quantum Field Theory* (Westview Press, 1995).
- [2] M. D. Schwartz, *Quantum Field Theory and the Standard Model* (Cambridge University Press, 2014).
- [3] A. Purcell, [CERN Bulletin](#) **35**, 10 (2012).
- [4] S. L. Glashow, [Nuclear Physics](#) **22**, 579 (1961).
- [5] A. Salam, *8th Nobel Symposium Lerum, Sweden, May 19-25, 1968*, Conf. Proc. **C680519**, 367 (1968).
- [6] S. Weinberg, [Phys. Rev. Lett.](#) **19**, 1264 (1967).
- [7] F. Englert and R. Brout, [Phys. Rev. Lett.](#) **13**, 321 (1964).
- [8] P. W. Higgs, [Phys. Rev. Lett.](#) **13**, 508 (1964).
- [9] G. S. Guralnik, C. R. Hagen, and T. W. B. Kibble, [Phys. Rev. Lett.](#) **13**, 585 (1964).
- [10] W. de Boer (CMS), in *Time and Matter 2013 (TAM2013) Venice, Italy* (2013) [arxiv:1309.0721 \[hep-ph\]](#).
- [11] M. Tanabashi *et al.* (Particle Data Group), [Phys. Rev. D](#) **98**, 030001 (2018).
- [12] J. Goldstone, [Il Nuovo Cimento \(1955-1965\)](#) **19**, 154 (1961).
- [13] D. de Florian *et al.* (LHC Higgs Cross Section Working Group), (2016), [10.23731/CYRM-2017-002](#), [arxiv:1610.07922 \[hep-ph\]](#).
- [14] ATLAS Collaboration, [Phys. Lett. B](#) **716**, 1 (2012), [arxiv:1207.7214](#).
- [15] CMS Collaboration, [Phys. Lett. B](#) **716**, 30 (2012), [arxiv:1207.7235](#).
- [16] ATLAS Collaboration, [Phys. Lett. B](#) **726**, 120 (2013).
- [17] CMS Collaboration, [Phys. Rev. Lett.](#) **110**, 081803 (2013).
- [18] ATLAS and CMS Collaborations, [Journal of High Energy Physics](#) **2016**, 45 (2016).
- [19] CMS Collaboration, [Phys. Rev. Lett.](#) **120**, 071802 (2018).
- [20] J. Campbell, K. Ellis, W. Giele, T. Neumann, and C. Williams, “[MCFM - Monte Carlo for FeMtobarn processes,](#)” (2018).
- [21] CMS Collaboration, “[Summaries of CMS cross section measurements,](#)” (2018).
- [22] ALEPH, DELPHI, L3, and OPAL Collaborations, [Phys. Lett. B](#) **565**, 61 (2003).

- [23] CDF and D0 Collaborations, *Phys. Rev. Lett.* **109**, 071804 (2012).
- [24] ATLAS Collaboration, *Journal of High Energy Physics* **2015**, 69 (2015).
- [25] CMS Collaboration, *The European Physical Journal C* **75**, 212 (2015).
- [26] ATLAS and CMS Collaborations, *Journal of High Energy Physics* **2016**, 45 (2016).
- [27] ATLAS Collaboration, *Journal of High Energy Physics* **2017**, 24 (2017).
- [28] CMS Collaboration, *Physics Letters B* **780**, 501 (2018).
- [29] P. Mouche, *Overall view of the LHC. Vue d'ensemble du LHC* (2014).
- [30] J. Haffner, *The CERN accelerator complex. Complexe des accélérateurs du CERN* (2013).
- [31] J.-L. Caron, “Cross section of LHC dipole. Dipole LHC: coupe transversale.” (1998).
- [32] J.-L. Caron, “LHC quadrupole cross section.” (1998).
- [33] CMS Collaboration, *CMS Physics: Technical Design Report Volume 1: Detector Performance and Software*, Technical Design Report CMS (CERN, Geneva, 2006).
- [34] T. Sakuma and T. McCauley, *Detector and event visualization with SketchUp at the CMS experiment*, Tech. Rep. CMS-CR-2013-379. arxiv:1311.4942 (CERN, Geneva, 2013).
- [35] R. Breedon *et al.*, “CSC Strip, Wire, Chamber, and Electronics Conventions,” (2007).
- [36] D. Barney, “CMS Detector Slice.” (2016).
- [37] CMS Collaboration, *Phys. Rev. D* **89**, 012003 (2014).
- [38] CMS Collaboration, *Phys. Rev. Lett.* **121**, 121801 (2018).
- [39] D. Kovalskyi, M. Tadel, A. Mrak-Tadel, B. Bellenot, V. Kuznetsov, C. D. Jones, L. Bauerdick, M. Case, J. Mülsenstädt, and A. Yagil, *Journal of Physics: Conference Series* **219**, 032014 (2010)

## BIOGRAPHICAL SKETCH

Sean-Jiun Wang was born in West Palm Beach, Florida. After graduating from Suncoast High School with an interest in physics, he attended the University of Florida where he obtained a Bachelor of Science in physics and mathematics. For his graduate education, he remained at the University of Florida to pursue experimental high energy physics. Upon completing his coursework, he moved to the Franco-Swiss border where he began his graduate research with the CMS experiment at CERN. A year later, he was awarded the 2016 LPC Graduate Scholar fellowship and moved to Fermi National Accelerator Laboratory in Illinois where he would work closely with his advisor Dr. Jacobo Konigsberg until the end of his graduate research. He received a Doctor of Philosophy in the spring of 2019.